

# An XMM-Newton View of the ANdromeda Galaxy as Explored in a Legacy Survey (New-ANGELS) I: the X-ray Source Catalogue

RUI HUANG,<sup>1</sup> JIANG-TAO LI,<sup>2</sup> WEI CUI,<sup>1</sup> JOEL N. BREGMAN,<sup>2</sup> XIANG-DONG LI,<sup>3,4</sup> GABRIELE PONTI,<sup>5,6</sup> ZHIJIE QU,<sup>7</sup>  
Q. DANIEL WANG,<sup>8</sup> AND YI ZHANG<sup>5</sup>

<sup>1</sup>*Department of Astronomy, Tsinghua University, Beijing 100084, China*

<sup>2</sup>*Department of Astronomy, University of Michigan, 311 West Hall, 1085 S. University Ave, Ann Arbor, MI, 48109-1107, U.S.A.*

<sup>3</sup>*School of Astronomy and Space Science, Nanjing University, Nanjing 210023, People's Republic of China*

<sup>4</sup>*Key Laboratory of Modern Astronomy and Astrophysics, Nanjing University, Ministry of Education, Nanjing 210023, People's Republic of China*

<sup>5</sup>*INAF-Osservatorio Astronomico di Brera, Via E. Bianchi 46, 23807 Merate (LC), Italy*

<sup>6</sup>*Max-Planck-Institut für Extraterrestrische Physik, Giessenbachstrasse, 85748 Garching, Germany*

<sup>7</sup>*Department of Astronomy & Astrophysics, The University of Chicago, Chicago, IL 60637, U.S.A*

<sup>8</sup>*Department of Astronomy, University of Massachusetts, Amherst, MA 01003, U.S.A.*

## ABSTRACT

We introduce the New-ANGELS program, an *XMM-Newton* survey of  $\sim 7.2$  deg<sup>2</sup> area around M 31, which aims to study the X-ray populations in M 31 disk and the X-ray emitting hot gas in the inner halo of M 31 up to 30 kpc. In this first paper, we report the catalogue of 4506 detected X-ray sources, and attempt to cross-identify or roughly classify them. We identify 352 single stars in the foreground, 35 globular clusters and 27 supernova remnants associated with M 31, as well as 62 AGNs, 59 galaxies, and 1 galaxy clusters in the background. We uniquely classify 236 foreground stars and 17 supersoft sources based on their X-ray colors. X-ray binaries (83 LMXBs, 1 HMXBs) are classified based on their X-ray colors and X-ray variabilities. The remaining X-ray sources either have too low S/N to calculate their X-ray colors or do not have a unique classification, so are regarded as unclassified. The X-ray source catalogue is published online. Study of the X-ray source populations and the contribution of X-ray sources in the unresolved X-ray emissions based on this catalogue will be published in companion papers.

## 1. INTRODUCTION

X-ray studies of stellar sources provide a direct probe of the formation and evolution of different stellar populations (e.g., Fabbiano 2006). Compared to X-ray sources in the MW (e.g., Liu et al. 2007; Revnitvsev et al. 2007, 2011; Zhu et al. 2018) with large distance uncertainties (e.g., Jonker & Nelemans 2004), sources in a nearby galaxy are essentially at the same distance and are thus optimized to study the science based on accurate luminosity measurements [e.g., the X-ray source luminosity functions (Gilfanov 2004)]. For a local galaxy with a distance of a few Mpc and a typical *Chandra* or *XMM-Newton* exposure time of a few hundred ks, a point source detection limit of  $\sim 10^{36-37}$  ergs s<sup>-1</sup> in the 0.5-7 keV band, for example, is typically reached (e.g.,

Kim & Fabbiano 2004; Kim et al. 2009; Fabbiano 2006; Liu et al. 2007; Revnitvsev et al. 2008; Lehmer et al. 2010; Mineo et al. 2012). This detection limit is insufficient to characterize the properties of individual X-ray binaries down to the LF break at  $\lesssim 10^{37}$  ergs s<sup>-1</sup> (e.g., Gilfanov 2004). Most nearby galaxies with moderate X-ray observations only have about  $\sim 10^2$  detected X-ray sources (e.g., Irwin et al. 2002; Li et al. 2008; Li & Wang 2013a), which is too few for many follow-up analyses, such as estimating the X-ray-stellar mass ratio ( $N_X/M_*$  or  $L_X/M_*$ ; the latter could be highly biased by one or two luminous X-ray sources; e.g., Revnitvsev et al. 2008; Lehmer et al. 2010). This highlights the importance of an X-ray survey of a nearby galaxy to a detection limit as low as  $\lesssim 10^{36}$  ergs s<sup>-1</sup>.

The Andromeda galaxy M 31 is the closest massive spiral galaxy to the MW (distance  $d = 761$  kpc,  $5'' \approx 18$  pc; Li et al. 2021b). It is the most massive galaxy in the Local Group and one of the most massive spiral galaxy in the local Universe, with a stellar mass of

$M_* = (1 - 1.5) \times 10^{11} M_\odot$  and a dark matter halo mass of  $M_{200} = (8 - 11) \times 10^{11} M_\odot$  (Tamm et al. 2012). M31 is very quiescent in star formation, with a star formation rate of only  $\text{SFR} \sim 0.4 M_\odot \text{ yr}^{-1}$  (Barmby et al. 2006). The Galactic foreground absorption toward M31 ( $N_{\text{H}} \sim 5 \times 10^{21} \text{ cm}^{-2}$ ) is not too high (HI4PI Collaboration et al. 2016). The small distance, large stellar and gravitational mass, low SFR, and large galactic disk inclination make M31 ideal to study the population, luminosity function, and vertical distribution of old stellar X-ray sources in a large luminosity range.

X-ray sources toward the direction of M31 has been extensively studied with various X-ray telescopes (e.g., van Speybroeck et al. 1979; Trinchieri & Fabbiano 1991; Supper et al. 1997, 2001), especially the bulge (e.g., Voss & Gilfanov 2007, Stiele et al. 2008) and disk area (e.g., Kong et al. 2003, Sasaki et al. 2018). The first catalogue of the *XMM-Newton* survey of M31 was published by Pietsch et al. (2005b), which consisted of 856 sources. Stiele et al. (2011) then updated the catalogue which contains 1948 sources. However, these observations toward the disk and bulge are insufficient to characterize the spatial variation of X-ray sources over large physical scales, which could be affected by the formation, evolution, and migration of different source populations (e.g., Zuo et al. 2008).

An *XMM-Newton* View of the **A**Ndromeda **G**alaxy as **E**xplored in a **L**egacy **S**urvey (New-ANGELS) is a legacy X-ray survey of the M31 disk and bulge, as well as its inner halo around the disk. The program is based on an *XMM-Newton* AO-16 large program surveying the M31 halo at  $r \lesssim 30 \text{ kpc}$  (PI: Li, Jiang-Tao), plus many archival data mainly covering its disk and bulge (Figs. 1, 2; Table A.1). The major scientific goals include not only the population, spatial distribution, and X-ray/IR ratio of stellar sources, but also the survey of foreground/background sources, as well as the large-scale diffuse X-ray emission from the hot gas (e.g., Li & Wang 2007, Bogdán & Gilfanov 2008, Bogdán & Gilfanov 2010, Kavanagh et al. 2020), the hot CGM potentially produced by accretion instead of galactic feedback in a representative massive quiescent spiral galaxy (e.g., Li et al. 2016, 2017, 2018).

As the first paper of the New-ANGELS project, we herein present by far the most comprehensive X-ray source catalog extracted from a  $\approx 7.2 \text{ deg}^2$  field around M31, down to a flux limit of  $F_{1.0-2.0\text{keV}} = 3.6 \times 10^{-15} \text{ ergs s}^{-1} \text{ cm}^{-2}$  (reached in 90% of the sky area covered in the survey) and the luminosity limit of  $L_{1.0-2.0\text{keV}} = 2.5 \times 10^{35} \text{ ergs s}^{-1}$  for M31 sources. Further statistical analysis and scientific discussions based on this X-ray source catalog (X-ray source LFs, spatial

distribution, and the X-ray/IR ratio of different X-ray source populations), as well as analysis of the diffuse X-ray emission from the hot gas, will be presented in follow-up papers. The present paper is organized as follows: In §2, we introduce the *XMM-Newton* observations used in the New-ANGELS project, as well as the data reduction and source detection procedures. We then discuss the source identification and classification based on either the multi-wavelength cross-identification or the multi-band color and/or extent in §3. The complete source catalog is described in detail in §4. All errors are quoted at  $1 \sigma$  confidence level throughout the paper unless specially noted.

## 2. OBSERVATIONS AND DATA REDUCTION

In order to have a complete survey of the X-ray sources in and around M31, we make use of all the available *XMM-Newton* observations which have a pointing position within the projected radius  $r \leq 30 \text{ kpc}$  ( $\approx 2.2^\circ$ , adopting a distance of  $d = 761 \text{ kpc}$ ; Li et al. 2021b) around the center of M31. In summary, there are 137 observations matching our selection criteria, but 28 of them are significantly impacted by strong background flares. Eleven observations pointing to the center of M31, with less than 20 ks of exposure time, are excluded as the central region already had sufficient exposure time, resulting in a final selection of 98 observations for subsequent analysis. Table A.1 in Appendix A provides a summary of them. The total/net (after removing strong background flares) exposure time is  $\approx 3.1/2.5$ ,  $3.1/2.6$ , and  $2.7/1.9 \text{ Ms}$  for MOS-1, MOS-2, and PN, respectively. The mosaicked *XMM-Newton* exposure map of all the observations is presented in Fig. 1.

We reprocess the *XMM-Newton* data using the *XMM-Newton* Science Analysis Software (SAS) v19.1.0. SAS does not have a fixed version of calibration files. Instead, these files are updated continuously. We use the latest calibration files until May 2022. We first reproduce the event lists of the three EPIC cameras (MOS-1, MOS-2, and PN) using the SAS tools `emchain` and `pnchain` for MOS and PN, respectively. We then identify and tag the MOS CCDs which are in anomalous states with `emtagnoise`. The registered events from these tagged CCDs are removed in the following analysis. We identify good time intervals (GTIs) by removing strong background flares mainly caused by elevated soft proton contamination using `mos-filter` and `pn-filter`. We further filter the events with the `#XMMEA_EM` filter in `evselect` for MOS and “FLAG == 0” for PN which provide a canned screening set of FLAG values for the event. These filters exclude ‘wrong’ or ‘suspicious’ events, e.g., near hot pixels or outside the field of

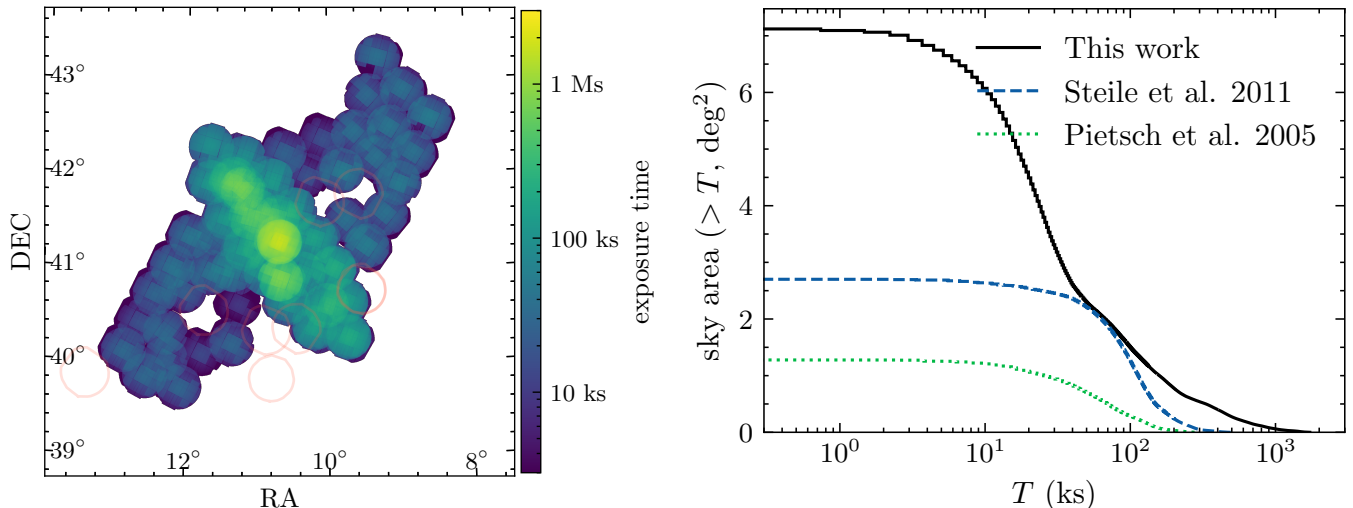


**Figure 1.** Left: All-EPIC exposure map of the *XMM-Newton* observations around M31. The color denotes the effective exposure time accounting for the vignetting. The pink circles represent observations that are excluded from data reduction and analysis due to background flaring. Right: The sky coverage of the observations above the given all-EPIC exposure time. The sky coverage of this work, Stiele et al. (2011), and Pietsch et al. (2005b) are shown in black solid line, blue dashed line, and green dotted line, respectively.

view (FOV) of the telescope. The GTIs of different observations (identified with the observation ID: ObsID) after these cleanings are summarized in Table A.1.

After reprocessing the event list, we perform standardized EPIC source detection with the task `edetect_stack`<sup>1</sup> (Traulsen et al. 2019, 2020) in five bands: 0.2-0.5 keV, 0.5-1.0 keV, 1.0-2.0 keV, 2.0-4.5 keV, and 4.5-12.0 keV, which are the standard bands used in many *XMM-Newton* catalogues (e.g., the 4XMM-DR12 catalog; Webb et al. 2020). The count rates measured in these bands are also used to define the hardness ratios of the source. The hardness ratio is defined as  $HR_i = (R_{i+1} - R_i)/(R_{i+1} + R_i)$ , where the  $R_1, R_2, R_3, R_4$ , and  $R_5$  are the count rates of all-EPIC in 0.2-0.5 keV, 0.5-1.0 keV, 1.0-2.0 keV, 2.0-4.5 keV, and 4.5-12.0 keV, respectively. `edetect_stack` is a tool chain to perform source detection on multiple mosaicked or stacked observations. It greatly improves the sensitivity of the source detection in the overlapping areas of different observations. Considering the efficiency, the source detection `edetect_stack` is not applied to the entire New-ANGLES footprint. Instead, we split the *XMM-Newton* survey area around M31 into five smaller areas (North, South, East, West, and Center, as summarized in Table 1 and plotted in different colors in Fig. 3) and perform source detection separately in each of them. For each of these five areas, we only include observa-

**Table 1.** Definition of sky areas used for source detection

Region	Definition
North	$d1 \geq 30'$
South	$d1 \leq -30'$
East	$-30' < d1 < 30', d2 < 0'$ and $R > 12'$
West	$-30' < d1 < 30', d2 \geq 0'$ and $R > 12'$
Center	$R \leq 12'$

NOTE— $d1$ ,  $d2$ , and  $R$  are the angular distance to the major axis, minor axis, and center of M31, assuming the position angle of M31 is  $37.3^\circ$ . Source detected in these different areas are plotted in different colors in Fig. 3.

tions whose pointing direction is within or  $\leq 10'$  from the boundary of different areas in the source detection procedure.

We use `edetect_stack` to detect sources with a two-stage procedure. We first run `edetect_stack` to the original cleaned data, which calls `evselect`, `eexpmap`, and `emask` to create the counts, exposure, and mask maps, respectively. We further modify the mask maps to limit the source detection area within the boundary as defined in Table 1 and Fig. 3 to speed up the source detection. In the second stage, we run `edetect_stack` again to perform the source detection within the five sub-areas, separately. It first calls `eboxdetect` to search sources in two steps: in the first step we use a local background to detect and remove the sources, then create global background maps; while in the second step,

<sup>1</sup> <http://xmm-tools.cosmos.esa.int/external/sas/current/doc/eboxdetect/>



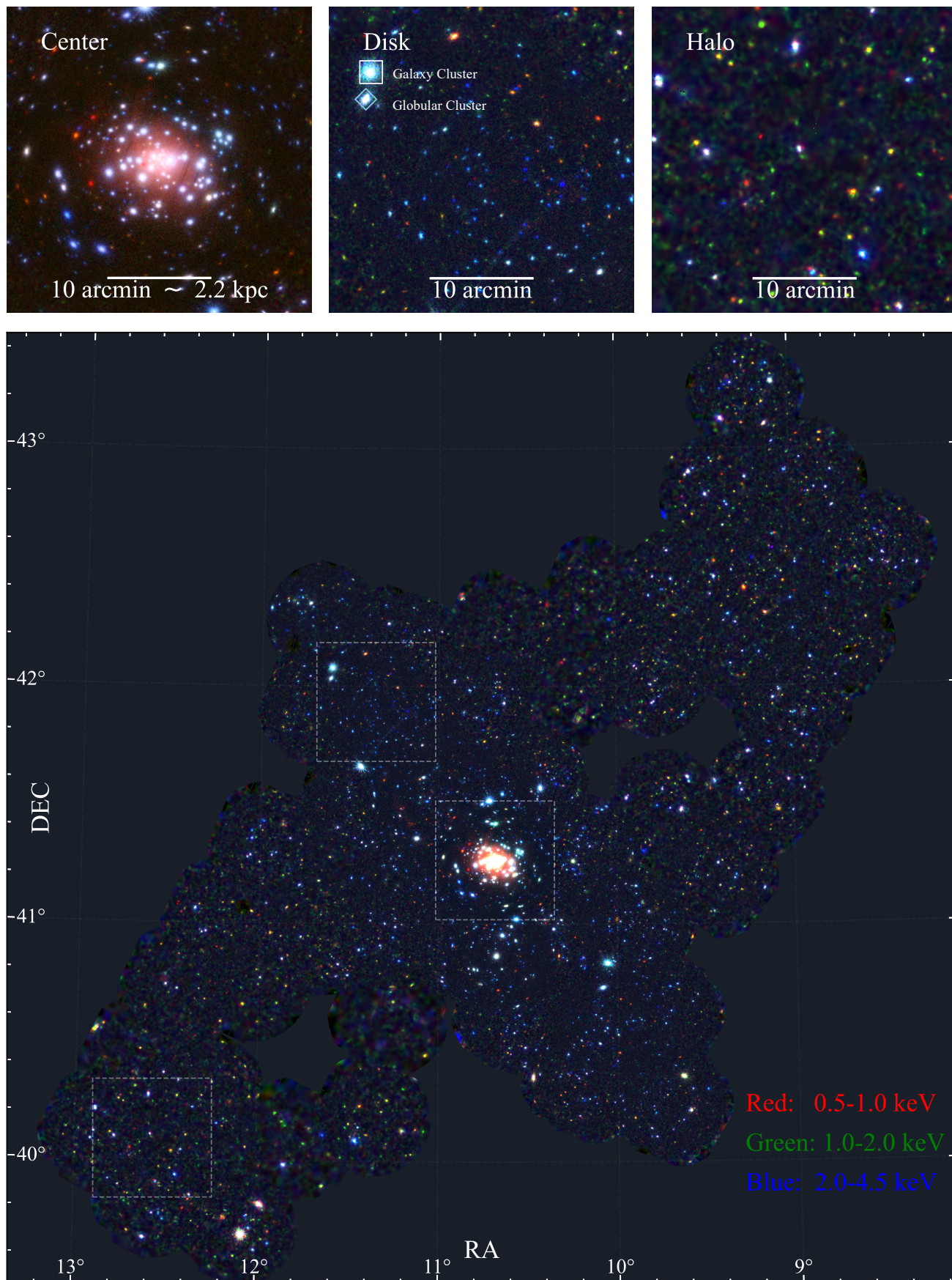


**Figure 2.** Mosaicked false-color image of the *XMM-Newton* observations of M31. We also show three zoom-in  $30' \times 30'$  regions in the center, disk, and halo. The count rate images are background subtracted, exposure corrected, adaptively smoothed, but not vignetting corrected. The scale bars of  $10' = 2.2$  kpc in the inserted panels are calculated at the distance of M31 (761 kpc). Because the center region is much brighter, we adjust the color scale of the upper left panel to capture more details.



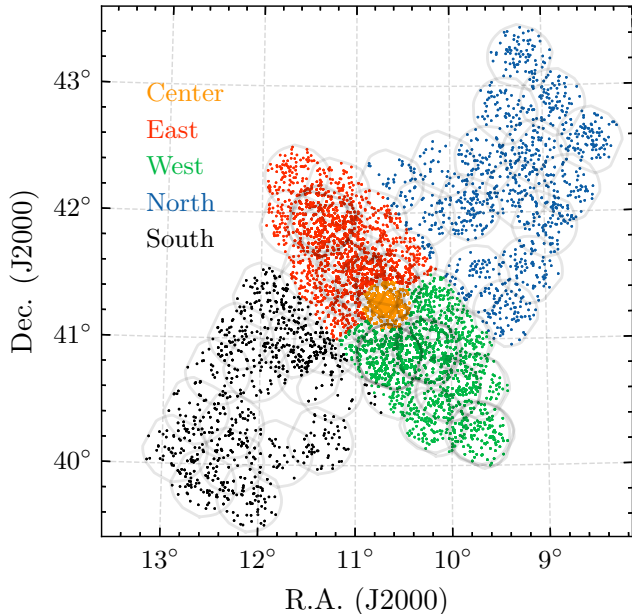


**Figure 3.** Location of detected X-ray sources. Sources detected in different areas as defined in Table 1 are plotted in different colors.

we use these global background files to perform sliding box search again. After this initial source searching, `edetect_stack` then calls `emldetect` to acquire the parameters of the sources by performing joint maximum likelihood point spread function (PSF) fitting on all the involved images of the given source simultaneously (see more detail in Traulsen et al. 2019, Traulsen et al. 2020). `edetect_stack` then produce the final EPIC summary source list by calling `srcmatch`.

Sometimes a faint source could fall into the gaps or bad pixels of one of the three EPIC cameras. In this case, `edetect_stack` still performs maximum likelihood multi-source PSF fitting (by calling `emldetect`) at the same position based on the detection on the other one or two cameras. It may obtain a zero flux of the source on a certain camera. This will significantly bias the final parameters of the source in the summary list. Therefore, we mark the ‘zero flux’ of detected sources as non-detection due to their falling into the CCD gaps or bad pixels in one or two cameras. We then recalculate the combined parameters of the sources based only on the detection on other cameras (flux, detection likelihood with an updated degree of freedom, etc.).

### 3. X-RAY SOURCE IDENTIFICATION AND CLASSIFICATION

M31 is unique for systematic studies of different populations of X-ray sources either associated with the galaxy or in the foreground/background (e.g., Fabbiano 2006),

including low- and high-mass X-ray binaries (LMXBs and HMXBs), ultra-luminous X-ray sources (ULXs), and other accreting or non-accreting stellar binary X-ray sources (e.g., supersoft sources, SSSs), open or globular clusters, isolated neutron stars and magnetars, supernova remnants (SNRs) and pulsar wind nebulae (PWNe), background galaxies/groups/clusters, AGN, and transient X-ray sources (e.g., SNe, GRB), etc. In this section, we will identify or classify the detected X-ray sources around M31 in two ways: either by identification of the sources based on cross-matching them with other firmly identified multi-wavelength counterparts (§3.2), or by rough classification of the sources based on their multi-band (including X-ray) colors, morphology, and/or variability (§3.3). The former way is often a firm unique identification of the nature of the source, while the latter one is just a rough classification of the source, and a single source may be classified as candidates of different types of objects.

#### 3.1. Multi-wavelength catalogues and cross-match criteria

We compare our *XMM-Newton* source catalogue in and around M31 to other multi-wavelength catalogues to cross-identify the sources. The multi-wavelength catalogues used in the cross-identification include (as summarized in Table 2): the SIMBAD (Wenger et al. 2000), Pan-STARRS (PS1) DR1 (Chambers et al. 2016), and AllWISE (Cutri et al. 2021) databases for various types of objects; the Local Group Galaxies Survey (LGGS; Massey et al. 2006) for optical sources on the M31 disk; GAIA DR3 for stars (Gaia Collaboration et al. 2016, 2021); the Revised Bologna Catalog (Galleti et al. 2004) for globular clusters (GICs); Jennings et al. (2014) and Lee & Lee (2014) for SNRs; the Million Quasars (Milliquas) catalog v7.2 (an update of Flesch 2015) for AGN.

We adopt different cross-match criteria for different types of sources based on their different spatial extension and multi-wavelength properties. Details of the cross-identification procedure for different types of sources will be described in §3.2.1, 3.2.2, and 3.2.3, while a brief summary of the criteria is listed in Table 2. In most of the cases, we define the cross match criteria based on the X-ray position uncertainty  $\sigma_{\text{pos}}$  of the *XMM-Newton* sources (joint fit in five bands), which is determined via PSF fitting. To include the additional position uncertainty, we use the following empirical formula:

$$\sigma_{\text{combined}} = \sqrt{0.89 \times \sigma_{\text{pos}}^2 + 0.42^2} \quad (1)$$

More information can be found in Appendix B. For most of the point-like sources, we cross match the multi-wavelength counterparts with  $\Delta_{\text{pos}} < 3.44\sigma_{\text{combined}}$

from the detected X-ray sources. For extended sources such as galaxies, galaxy clusters, or SNRs, however, in addition to an initial cross-match in a larger radial range, we manually check each cross-matched sources on the multi-wavelength images to avoid mis-match.

A more complicated case is the foreground (fg) star, which we use the Gaia DR3 catalogue to identify (Gaia Collaboration et al. 2016, 2021). As the number density of foreground star is very high, we often identify multiple stars within  $3.44 \sigma_{\text{combined}}$  from the X-ray sources. We therefore adopt a different procedure to cross match the stars to our X-ray sources. We generate a foreground star catalogue from Gaia DR3 with PSS > 90% (PSS is the column in GAIA DR3 referring to the probability as a single star). We then use the NWAY<sup>2</sup>(a Bayesian algorithm for cross-matching multiple catalogs, Salvato et al. 2018; Buchner et al. 2021) algorithm to cross-match the foreground stars to our X-ray catalogue by considering their X-ray/optical locations, the X-ray-to-optical flux ratio, and the X-ray hardness ratio HR2. Details of the cross-matching procedure is presented in the appendix (§C). We use the NWAY parameter p\_any which is the probability that the X-ray source has at least a reliable counterpart, instead of just the separation between the X-ray and optical sources, to describe the likelihood of a GAIA source being the counterpart of an X-ray source. Typically, p\_any > 0.9 corresponds to a false detection rate of < 5%.

### 3.2. Multi-Wavelength Cross Identification

There are basically three types of X-ray sources detected in the field: foreground sources which are mainly stellar sources (single or binary stars) in the MW, various types of X-ray sources associated with M 31 (SNRs, globular clusters, and many stellar sources), and distant sources in the background (AGN, galaxies, and galaxy clusters). The most reliable way to firmly identify these X-ray sources is often to search for their identified multi-wavelength counterparts, using the catalogues and cross-match algorithm described in the above section (§3.1). This is often more reliable than a simple classification of the sources based on their X-ray or multi-band colors or other multi-wavelength parameters (§3.3).

#### 3.2.1. Stellar X-ray sources in the foreground

Since M 31 is located in the direction off the Galactic plane, most of the foreground X-ray sources should be relatively old stars, including both single and binary stars in the MW. Although in principle we can also detect other types of sources such as SNRs or globular

clusters, they could in principle be easily identified and unlikely to be the dominant population in the direction of M 31 (in fact, we do not find any SNRs or globular clusters in the MW toward the direction of M 31 in our catalogue).

We will discuss the classification of binary X-ray sources in §3.3. Here we only focus on single star X-ray sources. Single stars tend to be individually faint in X-ray. Typically, K and M stars have  $L_X \lesssim 10^{29}$  ergs s<sup>-1</sup> (e.g., Schmitt et al. 1995). O, B stars can be as luminous as  $L_X \sim 10^{33}$  ergs s<sup>-1</sup> (e.g., Sana et al. 2006), which is marginally detectable at the distance of M 31 with very deep X-ray observations (the lowest detection limit toward the nuclear region of M 31 in our NEW-ANGELS project is  $L_{0.2-12 \text{ keV}} \sim 10^{34}$  ergs s<sup>-1</sup>; see Paper II for details). However, these young stellar populations are not expected to be located far away from the disk of the MW. Therefore, most of the X-ray emitting single stars cross-matched with the GAIA catalogue should be within the solar neighbourhood. We have firmly identified 352 X-ray sources as single stars in the GAIA catalogue, of which, 234 have a reliable distance measurement, and the median value is  $d = 434_{-207}^{+555}$  pc, confirming their nature as foreground sources.

Cautions should be made here that the GAIA catalogue does not distinguish single star and close binary stars, but simply call them “single stars” due to the dominance of single stars in the catalogue (Delchambre et al. 2022). We find some sources classified as “fg stars” in Table 2 have hard X-ray spectra (Fig. 4a), which may indicate some of them are actually accreting XRBs. Nevertheless, we still call fg stars identified in GAIA as “single stars” throughout the paper.

#### 3.2.2. GICs and SNRs associated with M 31

Most of the discrete X-ray sources associated with M 31 are neutron star or black hole accreting binaries. Most such binary systems are faint in optical and IR, so are identified mainly based on their X-ray properties (e.g., Stiele et al. 2011). Classification of these sources will be further discussed in §3.3. We herein only cross-identify two types of X-ray sources associated with M 31, GIC and SNRs, with the corresponding multi-wavelength catalogues.

X-ray emission from GICs is often contributed by various types of low-luminosity X-ray sources, [ $L_X < 10^{35}$  ergs s<sup>-1</sup>, including active binaries (ABs), cataclysmic variables (CVs), and millisecond pulsars (MSPs), and quiescent LMXBs, etc. (e.g., Heinke et al. 2005; Bahramian et al. 2020)] or dominated by accreting binaries. Such sources also tend to show significant X-ray variabilities (e.g., Heinke et al. 2005; Bahramian

<sup>2</sup> <https://github.com/JohannesBuchner/nway>

**Table 2.** Summary of the criteria and results of source identification and classification in and around M31

Type	Cross-Matched Catalogs	Identification	Classification	Confirmed	Candidates
fg star	GAIA DR3	1. NWAY $p_{\text{any}}^a > 0.9$ ; 2. $PSS^b > 90\%$ ; 3. point source	1. soft <sup>c</sup> in X-ray; 2. not AGN or confirmed fg star; 3. point source	352	236
AGN	The Million Quasars (Milliquas) catalog, v7.2	$\Delta\text{pos} < 3.44\sigma_{\text{combined}}^d$ from a confirmed AGN	$\Delta\text{pos} < 3.44\sigma_{\text{combined}}$ from an AGN candidate	62	505
Globular cluster (GIC) in M31	Revised Bologna Catalog, v5; SIMABD	$\Delta\text{pos} < 3.44\sigma_{\text{combined}}$ from a confirmed GIC	$\Delta\text{pos} < 3.44\sigma_{\text{combined}}$ from a GIC candidate	35	0
Supernova remnant (SNR) in M31	Jennings et al. (2014); Lee & Lee (2014)	1. no AGN or confirmed fg star at $\Delta\text{pos} < 10''$ ; 2. $\Delta\text{pos} < 3.44\sigma_{\text{combined}}$ from a SNR candidate; 3. manual check	1. no AGN or confirmed fg star at $\Delta\text{pos} < 10''$ ; 2. $3.44\sigma_{\text{combined}} \leq \Delta\text{pos} < 10''$ from a SNR candidate; 3. manual check	27	4
Galaxy (Gal)	SIMABD	1. no AGN or confirmed fg star at $\Delta\text{pos} < 6''$ ; 2. $\Delta\text{pos} < 3.44\sigma_{\text{combined}}$ from a galaxy; 3. manual check	1. no AGN or confirmed fg star at $\Delta\text{pos} < 6''$ ; 2. $3.44\sigma_{\text{combined}} \leq \Delta\text{pos} < 6''$ from a galaxy; 3. manual check	59	3
Galaxy cluster (GCl)	SIMBAD	1. extended <sup>e</sup> source in X-ray; 2. close to a confirmed galaxy cluster based on manual check	1. extended source in X-ray; 2. close to a galaxy cluster candidate based on manual check	1	5
Super soft source (SSS)	N/A	1. $HR1 < 0$ , $HR2 < -0.9$ ; 2. point source	1. only detected in 0.2-0.5 keV; 2. point source	11	6
High mass X-ray binary (HMXB)	1. Pan-STARRS DR1; 2. LGGS	1. hard <sup>c</sup> in X-ray; 2. blue <sup>f</sup> in optical but not AGN or confirmed fg star; 3. coincided with OB association or strongly variable <sup>g</sup> ; 4. point source	see unclassified sources	1	0
Low mass X-ray binary (LMXB)	1. Pan-STARRS DR1; 2. LGGS	1. hard in X-ray; 2. red or no confirmed optical counterpart, but not AGN or confirmed fg star; 3. strongly variable; 4. point source	see unclassified sources	83	0
total classified (with unique classification)				631	759
unclassified (with no or more than one classification)		1. not uniquely classified; 2. low $S/N^h$ or extended	1. not uniquely classified; 2. hard in X-ray; 3a. blue in optical: AGN or HMXB; 3b. red or no confirmed optical counterpart: AGN or LMXB; 4. Additional labels added to distinguish AGNs and XRBs based on HR2 and HR3 <sup>i</sup> .	2327	789

The table summarizes the multi-wavelength catalogues used for cross-identification of different types of X-ray sources, as well as the criteria of identifying confirmed sources, or classifying source candidates. The number of different types of firmly identified or roughly classified sources are listed in the last two columns.



Table 2 —continued.

- a. We use the NWAY algorithm to match the GAIA sources to our X-ray sources, considering both the X-ray to optical flux ratio and the X-ray hardness (see text for details).  $p_{\text{any}}$  is the matching probability defined by NWAY. The false matching rate is  $< 5\%$  when  $p_{\text{any}} > 0.9$ .
- b. PSS (between 0 and 100%) is the parameter in GAIA defining the probability of a source being classified as a star.
- c. We define X-ray sources with  $\text{HR2} - \text{HR1} + 0.53 > 0$  ( $\leq 0$ ) as ‘hard’ (‘soft’). HR1 (HR2) is the X-ray hardness ratio between the 0.2-0.5 keV and 0.5-1.0 keV (0.5-1.0 keV and 1.0-2.0 keV) bands, as detailed in the §2.
- d.  $\sigma_{\text{combined}}$  is the modified position uncertainty defined in Equ. 1
- e. We define sources as “extended”, when the detected extent radius (**EXTENT**, see Appendix D) of sources exceed  $6''$ .
- f. We define Pan-STARRS counterpart with  $g - r > 0$  ( $< 0$ ) as ‘red’ (‘blue’).
- g. We define sources with  $\text{FLUXVAR} > 10$  as ‘strongly variable’.
- h. We only use HR1 and HR2 in high S/N detections to classify sources, when  $\sigma_{\text{HR1}} < 0.2$  and  $\sigma_{\text{HR2}} < 0.2$ , where  $\sigma_{\text{HR1}}$  and  $\sigma_{\text{HR2}}$  are the uncertainties in the measured HR1 and HR2.
- i. We prefer unidentified hard X-ray source with  $\text{HR3} + 1.1 \times \text{HR2} > 0$  as XRB.

et al. 2020). The integrated X-ray spectra of GICs often comprise both thermal and non-thermal components, with the former mainly from ABs and CVs while the latter from MSPs and LMXBs (e.g., Heinke et al. 2005; Zhao & Heinke 2022). Since GICs are bright and often well identified in optical, we cross match our X-ray catalogue with the Revised Bologna Catalog of M31 clusters (Galleti et al. 2014), with the criteria described in §3.1 and summarized in Table 2. We in total identified 35 X-ray bright GICs in M31.

SNRs are often characterized with a strong thermal plasma X-ray spectrum, although some young ones also have a non-thermal hard X-ray tail. There are  $\sim 300$  SNRs identified in the MW (Green 2019). A large fraction of them reside in the Galactic plane, so suffer from strong foreground extinction. Compared to the SNRs in the MW, studying SNRs in an external galaxy has the advantage of having a typically lower foreground extinction and a more accurate distance. Until now, there are at least a few hundred SNRs detected in external galaxies with multi-wavelength observations (e.g., Maggi et al. 2016, 2019; Bozzetto et al. 2017). M31 is one of the galaxies with the largest number of SNRs identified (e.g., Sasaki et al. 2012; Lee & Lee 2014), only after the face-on and star forming galaxy M33 (e.g., Long et al. 2010; White et al. 2019) and M83 (e.g., Blair et al. 2012, 2015). We merge the optical SNR catalogue of M31 from Jennings et al. (2014) and Lee & Lee (2014), resulting in 177 SNR candidates. Since SNRs are extended sources and the optical/X-ray morphologies are not necessarily well correlated with each other, in addition to an automatic cross match, we also manually check our *XMM-Newton* X-ray and LGGS (Massey et al. 2006) H $\alpha$  image to make sure there is an X-ray source associated with the SNR. We regard X-ray sources with a separation of  $\Delta_{\text{pos}} < 3.44\sigma_{\text{combined}}$  from an identified SNR as a firmly identified X-ray emitting SNR, while those with  $3.44\sigma_{\text{combined}} \leq \Delta_{\text{pos}} < 10''$  as an SNR candidate. We in total identify 27 X-ray emitting SNRs and 4 more candidates.

### 3.2.3. Background sources

Background X-ray sources are anything in the distant universe, including AGNs, normal galaxies, and groups/clusters of galaxies, etc. In principle, their number densities should have a uniform spatial distribution across a small sky area such as that covered by our NEWANGLES survey. The X-ray emission from a normal galaxy without an AGN is comprised of both a thermal hot gas and a non-thermal stellar source component (e.g., Mineo et al. 2012; Li & Wang 2013a). It is in principle distinguishable from an AGN based on their X-ray

hardness ratios, especially if the hot gas contribution is significant (see §3.3 for details). Groups of galaxies also have softer spectra compared to AGNs, and their X-ray emissions often appear as extended sources with the centroid offset from a galaxy (e.g., Sun et al. 2009). On the other hand, a galaxy cluster often has stronger X-ray emission from the hot gas than from the AGN, but the hot gas emission is often significantly harder than that of a galaxy (due to the higher temperature, e.g., Li & Wang 2013b), so not significantly distinguishable in X-ray hardness from an AGN. However, the X-ray emission of a galaxy cluster is usually extended, and the nearby cluster (e.g.,  $z < 0.5$ ) is always well identified in optical images. Therefore, it is often not difficult to distinguish these different types of background sources. There may be some difficulties in distinguishing AGNs and XBs just based on their X-ray properties measured with poor counting statistics, but it is quite straightforward to identify an X-ray AGN if it is already identified in other ways (e.g., with an optical spectrum; Lyke et al. 2020).

By cross-matching our X-ray catalog with the Milliwas catalogue (Flesch 2015), we identify 62 confirmed X-ray emitting AGNs and 504 candidates. Since many of the AGN candidates are identified based on their multi-band colors instead of the spectral properties, the identification of an X-ray counterpart makes them a higher chance to be a real AGN. Since our identification of the X-ray emitting AGN is mostly based on the existing AGN catalogues, many of the unclassified hard X-ray sources (especially in the North and South region) could in fact be unidentified AGNs in these catalogues.

By manually checking their multi-wavelength images (e.g. mostly optical and IR from SDSS, Pan-STARRS, WISE, and HST), we identify 59 X-ray emitting galaxies without an identified AGN, and three more candidates of galaxies. Some of these X-ray sources could be associated with multiple galaxies, so may actually be galaxy groups. Furthermore, we also identify five extended X-ray sources as GCI candidates, while only one is firmly identified as a galaxy cluster at  $z \sim 0.29$  (2E 171, Kotov et al. 2006). This firmly identified GCI is projected in the direction of the disk of M31, and appears as an extended hard X-ray source.

### 3.3. Classification of X-ray Sources Based on Their Multi-band Properties

In the above section (§3.2), we have firmly identified hundreds of single stars in the foreground, GICs and SNRs associated with M31, as well as AGNs, galaxies, and GCIs in the background in our *XMM-Newton* X-ray source catalogue. We have also less firmly identified

hundreds of candidates of all of these types of sources, except for fg stars (will be discussed below). The cross-identification is mostly based on multi-wavelength cross-match of different identified source catalogues and is in general reliable and unique. However, the total number of sources identified this way is only  $\lesssim 10^3$ , or  $\sim 20\%$  or the total number of X-ray detected sources. A rough classification of a larger fraction of the X-ray sources, even if not unique and less reliable, is critical in the follow-up statistical analysis of different source populations. In this section, we discuss how to classify the remaining X-ray sources based on their X-ray and/or multi-band colors, or the X-ray variability.

Among all 62 AGNs and 504 candidates, 160 have an X-ray flux  $F_{2-4.5 \text{ keV}} > 10^{-14} \text{ ergs s}^{-1}$  in the entire  $7.2 \text{ deg}^2$  area covered by our NEW-ANGELS survey, leading to a surface density of  $18.3 \text{ deg}^{-2}$ . This is only  $\sim 20\%$  of the prediction based on some cosmological surveys where most of the detected X-ray sources should be AGN (e.g., [Chen et al. 2018](#)). However, when we zoom in to the inner halo regions (North and South), the number density of all detected sources is comparable to that of those surveys, the huge difference between the number of classified and expected AGNs may be caused by the large number of unidentified AGNs, which may have poorer optical data and not included in the Milli-quas catalogue. Furthermore, most of the stellar X-ray sources, either single or binary stars, are also not unambiguously identified, unless they are foreground sources included in the GAIA catalogue. In many cases, the classifications of these AGNs and stellar X-ray sources may not be unique.

### 3.3.1. Types of stellar X-ray sources

Both single stars and binaries can be X-ray sources. Single stars are often too faint in X-ray to be individually detected at the distance of M 31, so have to be foreground sources (§3.2.1). On the other hand, binary X-ray sources have a broad X-ray luminosity range (e.g., [Gilfanov 2004](#)), so could be either foreground sources or associated with M 31. There are basically two types of stellar binary X-ray sources: accreting binaries whose X-ray emission is mainly powered by the accretion of materials from the companion star to the compact star, and non-accreting binary sources whose X-ray emission is mainly produced via other mechanisms such as the stellar corona activity.

The X-ray emission from a non-accreting binary could be produced by the magnetically driven coronal activities (e.g., [Güdel 2004](#)). These sources are often identified as chromospherically active binaries (ABs; e.g., [Sazonov et al. 2006](#)), whose soft X-ray emission shows strong vari-

ability in a timescale of a few hours, and the spectrum is characterized by a thermal plasma at a typical temperature of  $kT \sim 0.5 \text{ keV}$  (sometimes with more complex temperature distributions; e.g., [Revnivtsev et al. 2008](#); [Singh & Pandey 2022](#)). There are also many individually faint stars (either binary stars or single stars) with a thermal plasma X-ray spectrum but only individually detectable with deep X-ray observations within the MW (e.g., [Rosner et al. 1985](#); [Schmitt et al. 1995](#); [Sana et al. 2006](#); [Revnivtsev et al. 2009](#)). Most of these non-accreting binary X-ray sources cannot be individually detected at the distance of M 31, but could still collectively contribute to the unresolved X-ray emissions.

Accreting X-ray binaries include LMXBs, HMXBs, cataclysmic variables (CVs), and supersoft sources (SSSs), etc., depending on the mass of their donor stars and the nature of the accreting compact star (black hole, neutron star, and white dwarf; e.g., [Remillard & McClintock 2006](#); [Mukai 2017](#)). Some special types of X-ray sources, such as ULXs and probably the major X-ray emitting sources in GLCs, are also accreting X-ray binaries (e.g., [Voss & Gilfanov 2007](#)). The X-ray emission from an accreting binary is mainly produced in its accretion disk and corona, and appears to be a power law with a photon index typically in the range of  $\Gamma \sim 1.5 - 2.0$  ([Irwin et al. 2003](#); [Fabbiano 2006](#)). On the other hand, because the temperature of accretion disk around a black hole is expected to fall with the increasing mass of the accreting compact object (e.g., [Miller et al. 2004](#)), the intrinsic X-ray emission tends to be harder than an accreting SMBH (the photon index of an AGN is typically  $\Gamma \sim 2$ ; e.g., [Brightman et al. 2013](#); [Li et al. 2021a](#)). However, it is often not straightforward to distinguish an individual X-ray binary either in the foreground or associated with M 31 from a background AGN only based on their X-ray spectral slopes, due to the limited number of photons and the complex intrinsic absorption. Furthermore, there also exist some special types of accreting X-ray binaries whose X-ray emission is supersoft. These SSSs are accreting white dwarfs, but different from the CVs, their X-ray emission is mostly produced by steady nuclear fusion on the white dwarf's surface, instead of from the accretion disk (e.g., [Greiner 2000](#)).

Accreting X-ray binaries span a large range of X-ray luminosity, with some most luminous ones could be detected individually in nearby galaxies (e.g., [Gilfanov 2004](#)). Therefore, it is often not easy to distinguish if a source is foreground or associated with M 31 only based on its spectral shape and X-ray brightness, especially if the source is located outside the disk of M 31. Nevertheless, based on multi-wavelength cross-identifications,



there are various types of accreting X-ray binaries or candidates identified associated with M31 in the literature, such as LMXBs (e.g., Stiele et al. 2011; Sasaki et al. 2018), HMXBs (e.g., Shaw Greening et al. 2009; Williams et al. 2018; Dalcanton et al. 2012; Williams et al. 2014; Lazzarini et al. 2021), and SSSs (e.g., Pietsch et al. 2005b,a; Stiele et al. 2011; Sasaki et al. 2018). In particular, there are also two confirmed ULXs in M31: CXOM31 J004253.1+411422 ( $L_{0.2-10 \text{ keV}} \approx 3.8 \times 10^{39} \text{ ergs s}^{-1}$ ; Henze et al. 2009; Kaur et al. 2012) and XMMU J004243.6+412519 ( $L_{0.5-10 \text{ keV}} \approx 2.3 \times 10^{39} \text{ ergs s}^{-1}$ ; Henze et al. 2012; Esposito et al. 2013). In the next subsection (§3.3.2), we will introduce a systematic way to classify these stellar X-ray sources and AGNs.

### 3.3.2. X-ray source classification criteria

We first classify the X-ray sources based solely on their X-ray colors, which are defined with a few inter-band hardness ratios as defined in §2. Compared to spectral analysis which is often adopted for bright sources, these hardness ratios are especially helpful to roughly characterize the spectral shape of faint sources which have too few counts to extract a spectrum. A few X-ray color-color diagrams based on different hardness ratios are presented in Fig. 4, where we also overlay the expected locations of a few simple spectral models (APEC and power law) with different parameters (foreground absorption column density  $N_{\text{H}}$ , thermal plasma temperature  $kT$  of the APEC model, or photon index  $\Gamma$  of the power law model). Three different column densities in the figure represent typical  $N_{\text{H}}$  values of no absorption with  $N_{\text{H}} = 0 \text{ cm}^{-2}$ , Galactic foreground absorption to the direction of M31 with  $N_{\text{H}} \approx 5 \times 10^{20} \text{ cm}^{-2}$ , and the absorption of M31 disk with  $N_{\text{H}} \approx 3 \times 10^{21} \text{ cm}^{-2}$  which are estimated from HI4PI HI map (HI4PI Collaboration et al. 2016), respectively. Assuming either a power-law or APEC model, the absorption would cause X-ray sources to shift along the solid line shown in the color-color diagram (Fig. 4). Despite M31’s proximity to the Galactic plane (with a Galactic latitude of  $b = -21.4^\circ$ ), the amount of Galactic foreground absorption is not substantial enough to cause a significant shift in its position on the color-color diagram according to Fig. 4. All the data points plotted in Fig. 4 are the detected sources in M31 with the detection likelihood  $\text{EP\_DET\_ML} \geq 6$ , and the uncertainty on the measured hardness ratios  $\sigma_{\text{HR}} < 0.2$ . There are in total  $\sim 2000$  sources plotted in Fig. 4. We will only use these sources with a relatively high detection S/N to discuss the source classification criteria below. The remaining ones, if not already uniquely classified as fg stars, AGNs,

GICs, SNRs, galaxies, or GCs, will then be treated as unclassified sources (Table 2).

We first characterize the location of the identified X-ray sources in 4XMM-DR11s on the color-color diagram, and compare them to our firmly identified and classified sources around M31, in order to determine the source classification criteria. We cross-match the 4XMM-DR11s catalogue (e.g., Traulsen et al. 2020, 2022) with the SIMBAD catalogue to identify the X-ray sources, with a strict criteria of the separation between the sources in the two catalogues  $\Delta_{\text{pos}} < 1''$ . As there are too many identified sources matched to 4XMM-DR11s (18605 AGNs, 3446 galaxies, 7037 stars, 51 SNRs, 379 XRBs, 154 GICs), we plot the probability density distribution, instead of individual data points, of different types of sources in Fig. 4.

It is clear that different types of sources distribute in distinct areas in the X-ray color-color diagram (Fig. 4), although some populations are heavily overlapped. In general, AGNs, XRBs and GICs are hard in X-ray, while SNRs and fg stars are soft. These “hard” and “soft” sources are easy to distinguish. Galaxies have a wide distribution on the color-color diagram, and includes the area occupied by AGNs, indicating that some of the X-ray sources identified as galaxies may actually host an unidentified X-ray bright AGN. Most of the fg stars appear soft in X-ray. These sources are likely single stars or non-accreting binaries as introduced in §3.2.1 and 3.3.1. However, a significant fraction of fg stars have a hard X-ray spectrum consistent with that of XRBs. These sources may thus be unidentified accreting X-ray binaries instead of single stars (§3.2.1; Delchambre et al. 2022).

The contamination of AGNs and XRBs in the identification of galaxies and fg stars is more clearly shown in Fig. 5, where we plot the probability distribution of different types of sources in two X-ray color combinations obtained from the HR1-HR2 and HR2-HR3 diagrams. The dashed lines in the panels a and b of Fig. 5 ( $\text{HR2} - \text{HR1} + 0.53 = 0$ ,  $\text{HR3} + 1.1 \times \text{HR2} + 0.71 = 0$ ) are the same as those in Fig. 4a,b, separating the “hard” and “soft” sources. Notably, the criterion used in the HR1-HR2 diagram (Fig. 4a) is in line with the effect of absorption. Even when there is a significant amount of absorption, modifying the value of  $N_{\text{H}}$  would not substantially impact the classification of X-rays as either “hard” or “soft”. It is clear that galaxies have a similar peak position in X-ray colors as AGNs, but a significantly broader distribution. This similar peak position indicates many galaxies should indeed host an unidentified AGN. Despite XRBs would dominate the emission of galaxies, the peak of galaxies shown in Fig. 4b is still

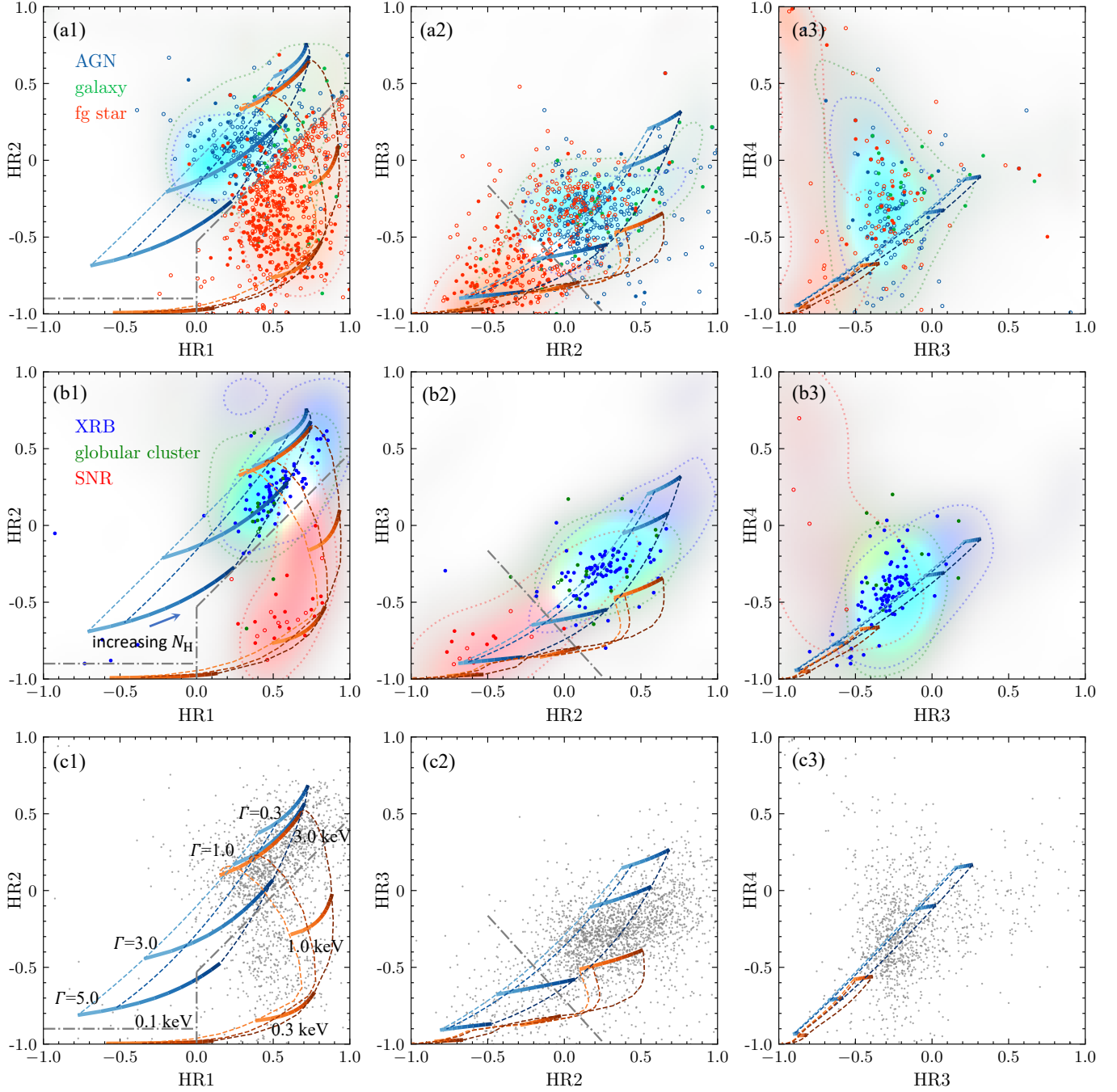


**Figure 4.** Color-color diagram of the detected X-ray sources with HR errors  $\sigma_{\text{HR}} < 0.2$ . Identified fg stars, AGNs and galaxies are plotted in the top panels (a1, a2 and a3), with the firmly identified ones plotted in filled circle, while candidates in open circles. Identified globular clusters, XRBs and SNRs are plotted in the middle panels (b1, b2 and b3). All the sources detected in the present work are plotted in the bottom panels (c1, c2 and c3). The underlying false-color images are the probability distribution of the cross-matched sources between 4XMM-DR11s (Traulsen et al. 2020, 2022) and SIMBAD (top row: AGN in blue, galaxy in green, fg star in red; middle row: XRB in blue, globular cluster in green, SNR in red). The dotted contours enclose 68% of the cross-matched sources. We also overlay different power-law (in blue) and APEC (in red) models in the mesh grids. The color of the thick solid curves denote  $N_{\text{H}}$ , which changes from 0 to  $3 \times 10^{21} \text{ cm}^{-2}$ , with the three dashed curves mark  $N_{\text{H}} = 0, 5 \times 10^{20}$ , and  $3 \times 10^{21} \text{ cm}^{-2}$ , respectively. The upper limit of  $N_{\text{H}}$  is roughly consistent with the peak value in the M31 disk. When computing the models, the response files of PN, MOS-1 and MOS-2 are used for the top, middle, and bottom rows, respectively. The dash-dotted lines show our criteria to classify different types of objects (SSSs, “hard” and “soft” sources; see Table 2 for details)

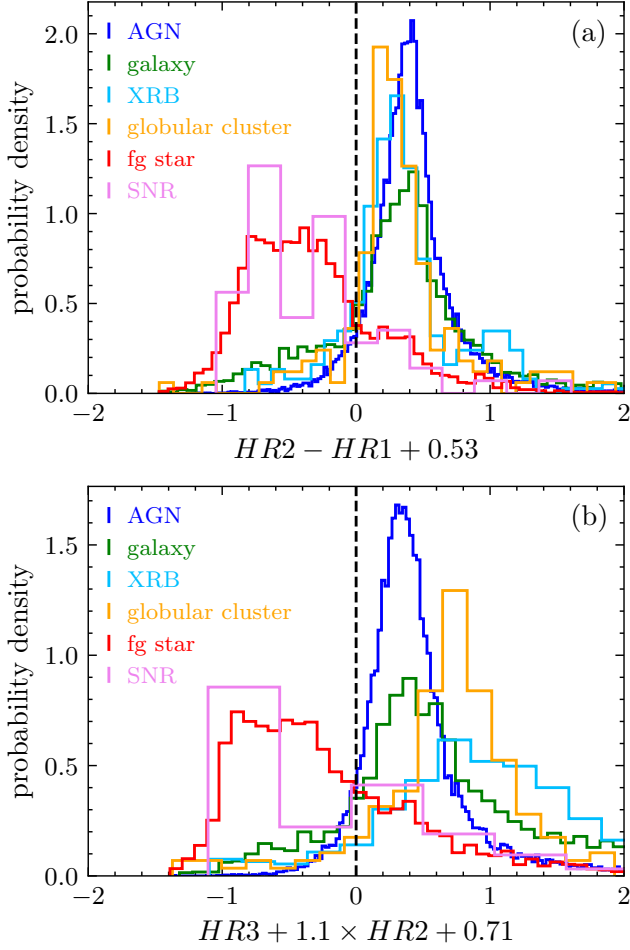


**Figure 5.** The probability density distribution of different types sources in Fig 4 at different hardness ratios. The vertical dashed lines mark our criteria to separate fg star v.s. AGN and XRB. The HR1-HR2 criterion in the upper panel is used in the source classification as summarized in Table 2.

in line with that of AGNs. On the other hand, fg stars, although the peak in the soft X-ray color domain, have a very asymmetric probability distribution, which is significantly biased to a harder tail. This hard tail should reflect the contribution from unidentified binary stars. Meanwhile, as indicated by Fig. 5b, XRBs tend to be harder than AGNs.

In addition to the “hard” and “soft” sources, we also identify some supersoft sources in Fig. 4. These three category of sources are defined as:

- Hard:  $HR1 - HR2 < 0.53$  and  $HR2 > -0.5$  in the HR1-HR2 diagram;  $HR3 + 1.1 \times HR2 > -0.71$  on the HR2-HR3 diagram.
- Soft:  $HR1 - HR2 > 0.53$  and  $HR1 > 0$  in the HR1-HR2 diagram;  $HR3 + 1.1 \times HR2 < -0.71$  on the HR2-HR3 diagram.

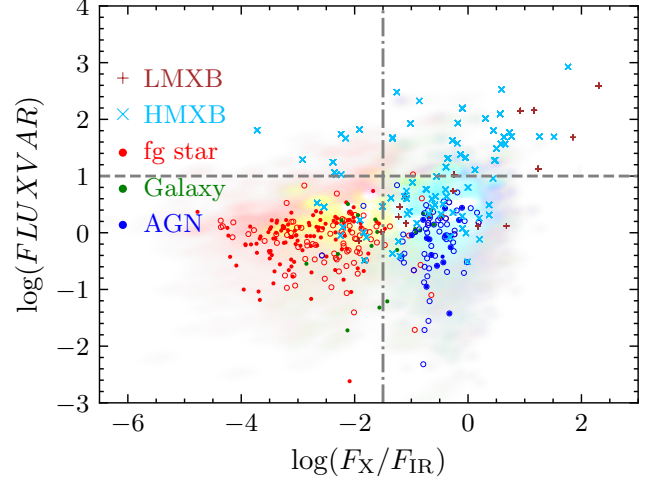


**Figure 6.** The X-ray to infrared flux ratio (X-ray flux calculated in 0.2-12 keV, while IR flux is the WISE 3.4  $\mu\text{m}$  flux) and X-ray variability of different X-ray source populations. Symbols are the same as in Fig. 4, except that the firmly identified LMXBs and HMXBs in the literatures (not limited to M31; e.g., Binder et al. 2015; Zhang et al. 2011) are plotted in plus and cross symbols. The vertical dash-dotted line roughly separates fg stars and AGN, while the horizontal dashed line defines “highly variable” sources, which is a key criterion to firmly identify XRBs (Table 2).

- Supersoft:  $HR2 < -0.9$  and  $HR1 < 0$  in the HR1-HR2 diagram. If a source is only detected in the 0.2-0.5 keV band and we cannot calculate HR2, it is also regarded as a candidate of SSSs (Table 2). Since SSSs are often not detected in the hard X-ray band, we do not define a criterion to identify them on the HR2-HR3 diagram.

Most ( $\approx 70\%$ ) fg stars and SNRs are “soft” sources, while most ( $\approx 90\%$ ) AGNs, galaxies, XRBs and GICs are “hard”. SSSs by definition are in the supersoft domain. They are often optical novae, or accreting white dwarfs, which often have a thermal spectrum with a temperature of  $kT \lesssim 100$  eV (e.g., Di Stefano et al. 2004; Pietsch et al. 2005a).

In addition to the X-ray colors, we also adopt the X-ray variability and the X-ray to IR flux ratio as two additional criteria to classify different types of sources. Here we characterize the variability of an X-ray source with the parameter FLUXVAR, which is the largest flux difference in terms of the standard deviation  $\sigma$  between multiple *XMM-Newton* observations (Table D). The 3.4  $\mu\text{m}$  IR flux of an X-ray source is taken from the AllWISE catalogue (Cutri et al. 2021). As shown in Fig. 6, the most variable X-ray sources are always XRBs, so we take  $\text{FLUXVAR} > 10$  as an additional criterion for firmly identified XRBs (Table 2), although many XRBs are indistin-



guishable from fg stars and AGNs in X-ray variability. AGNs and fg stars are also significantly distinguishable in the X-ray-IR color, we then use  $\log(F_X/F_{\text{IR}}) = -1.5$  (the vertical line in Fig. 6) as an auxiliary criterion to separate fg stars and AGNs. Although this criterion is not directly used in the classification of the sources, because fg stars and AGNs are often well separated in X-ray colors, our results are still reaffirmed, since our identified and classified fg stars and AGNs are also well separated by the  $\log(F_X/F_{\text{IR}}) = -1.5$ . So it is only used to place a caveat if the classification based on the X-ray color is thought to be less reliable, e.g., in case the source has a low S/N, or the two criteria based on the X-ray color and the X-ray-to-IR ratio are clearly conflict with each other.

### 3.3.3. Procedure to classify unidentified sources

Based on the above discussions, our final procedure to classify the *unidentified* X-ray sources (stellar sources and AGNs) in our NEW-ANGELS survey is summarized below (also see a summary in Table 2):

- We first cross-identify confirmed fg stars, confirmed or candidate AGNs, GICs, SNRs, galaxies, GCIs, based on their multi-wavelength counterparts (§3.2). The *XMM-Newton* data of some of these sources may not have high enough S/N to compute their X-ray colors with small uncertainties.

- For sources not identified in the above way, we calculate their X-ray colors HR1 and HR2. Sources with the uncertainties on HR1 and HR2  $\sigma_{\text{HR1}} \geq 0.2$  or  $\sigma_{\text{HR2}} \geq 0.2$  typically have low S/N, so are often regarded as unclassified, although we sometimes give them a preferred classification. Sources only detected in 0.2–0.5 keV are taken as candidates of SSSs.

- For relatively bright unclassified sources with  $\sigma_{\text{HR1}} < 0.2$  and  $\sigma_{\text{HR2}} < 0.2$ , we first classify them into “hard”, “soft”, and “supersoft” sources, based on their X-ray colors defined in §3.3.2. “Supersoft” sources are directly regarded as confirmed SSSs. “Soft” sources are directly taken as candidates of fg stars. The remaining “hard” sources are regarded as unclassified.

- For the “hard” unclassified sources, we further give them some preferred but non-unique classifications based on some additional multi-wavelength criteria. If the optical counterpart source is blue, they can be either HMXBs or AGNs, with their X-ray color defined with HR2 and HR3 being an additional criterion to assign the preferred classification. If the source is red in optical, or has no confirmed optical counterpart, they can be either LMXBs or AGNs, with the same X-ray color criterion to assign the preferred classification. We do not expect to match low-mass main sequence stars in M31,

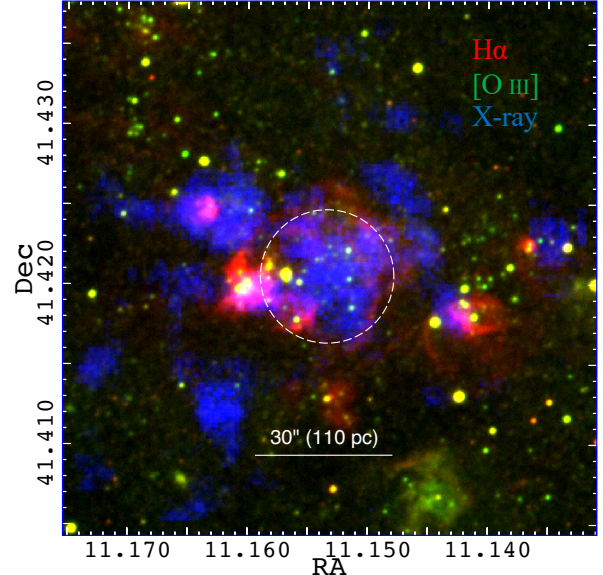


**Figure 7.** False-color image of the newly discovered super-bubble candidate J004436.8+412514. It is composed of H $\alpha$  (red), [O III]  $\lambda 5007\text{\AA}$  (green), and the X-ray (blue, 0.2 – 1.0 keV image which is smoothed with a 20 arcsec Gaussian kernel). A dashed circle with a diameter of 30'' ( $\sim 110$  pc at a distance of 761 kpc) has been superimposed on the location of the super bubble candidate.

but OB-type or giant stars are possible. Additionally, the possibility that the detected XRBS are foreground sources is not ruled out. Therefore, if no counterpart is found, the XRB is considered a LMXB. However, if a possible counterpart is found, the XRB is then classified as a HMXB or LMXB based on the color of the counterpart. Despite the potential for a false positive match due to the limited apparent magnitude of the actual donor star, a match can still offer insights into the environment of the XRB, such as the presence of a star-forming region.

- The above classification of some types of sources, e.g., the X-ray soft fg star candidates, could be largely uncertain. We then use some auxiliary criteria to add some caveats to their classification, such as the X-ray-to-IR flux ratio.

### 3.4. Noted sources of interest

In this section, we summarize a few noted X-ray sources which may be especially interesting in some aspects. This is only a very incomplete summary. We include some additional brief notes on many other sources in the final catalogue as will be described in §4.

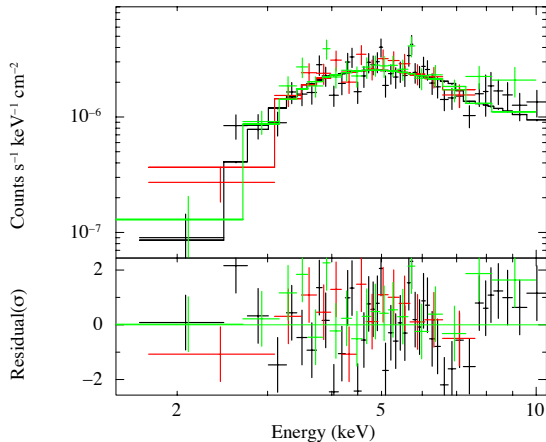


**Figure 8.** The stacked pn, mos1 and mos2 spectrum of AGN candidate J004442.8+415340 are shown in black, red and green respectively. Also shown are the corresponding best-fit absorbed power-law model and the residuals.

We discovered a  $\sim 110$  pc diameter superbubble candidate J004436.8+412514 in the eastern disk of M31 (Fig. 7). The extended soft X-ray emission is apparently enclosed by a few shells and filaments bright in optical emission lines such as  $H\alpha$  (optical images obtained from the LGGs project; Local Group Galaxies Survey, Massey et al. 2006). The overlapping location of the extended X-ray source and the  $H\alpha$  shell structure suggests the possible existence of a hot super bubble. The *XMM-Newton* spectra extracted from the entire bubble could be well fitted with an absorbed thermal plasma model (APEC, with  $N_H = 2.4 \times 10^{21} \text{ cm}^{-2}$ ,  $kT = 0.2 \text{ keV}$ ), the absorption corrected luminosity between 0.2-10 keV is  $1.1 \times 10^{37} \text{ erg s}^{-1}$ .

We detect a very hard point source J004442.8+415340 in the eastern disk direction of M31, with a  $HR3 = 0.96 \pm 0.02$ . The flux below 2 keV is negligible. The spectrum, as shown in Fig. 8, can be well modeled using an absorbed power-law with  $N_H = 1.7 \pm 0.2 \times 10^{23} \text{ cm}^{-2}$  and  $\Gamma = 1.9 \pm 0.3$ . The uncertainty is defined in the 90% confidence region. The measured flux (and unabsorbed flux) between 2-8 keV is  $1.2 \times 10^{-13} \text{ ergs s}^{-1} \text{ cm}^{-2}$  ( $3.0 \times 10^{-13} \text{ ergs s}^{-1} \text{ cm}^{-2}$ ). Our analysis suggests that the source is likely a moderately obscured AGN.

In this work, we detect eight extended X-ray sources associated with galaxies (see Fig. 9). Two of them (a,b) have unique single galaxy counterparts. The remaining six (c-h) have multiple galaxy counterparts and have potential to be galaxy groups. Four sources' counterparts (a-d) have measured redshift and are therefore confirmed to be background sources. The extended X-ray source J004133.4+422036 (a) has an apparent

soft X-ray luminosity of  $2.06 \times 10^{41} \text{ erg s}^{-1}$  at the distance of its counterpart 2MASXJ00413355+4220359 ( $z = 0.093$ , Caldwell et al. 2009). J003621.8+412836, associated with 2MASXJ00362166+4128333 at  $z = 0.064$  (Bilicki et al. 2014), has an apparent luminosity of  $3.7 \times 10^{40} \text{ erg s}^{-1}$ . For J004355.8+405854, the apparent luminosity of the detected extended source is  $3.49 \times 10^{40} \text{ erg s}^{-1}$  at a distance of  $z = 0.121$  (Caldwell et al. 2009), based on the redshift record of its counterpart NAME [G2012b]C039. J004253.1+414921 has an apparent luminosity of  $4.9 \times 10^{40} \text{ erg s}^{-1}$  at a distance of the counterpart 2MASXJ00414697+4138094 with  $z = 0.106$  (Galleti et al. 2007). This source also shows potential AGN activity based on its radio counterpart WSTB 37W145. In spite of the measured redshift, the limited luminosity of these sources excludes their possibilities as galaxy clusters. For the rest four extended X-ray source (e-h), the lack of measured redshift of the counterparts prevents estimation of their luminosity. These extended X-ray sources are still classified as galaxy in the catalogue, while we will note that they are extended and have one or more galaxy counterparts.

#### 4. X-RAY SOURCE CATALOG

In this paper, we present the most complete catalogue of 4506 X-ray sources detected from an area of  $\sim 7.2 \text{ deg}^2$  around M31 (Fig. 3). All reported sources have a limiting detection likelihood  $EP\_DET\_ML > 6$ , which leads to a false detection rate of  $< 0.5\%$  (e.g., Ni et al. 2021).

Stiele et al. (2011) detected 1948 X-ray sources in a comprehensive analysis of the archival XMM-Newton data covering the entire disk of M31. By incorporating 31 additional observations pointing slightly offset the disk of M31, we detect 2776 sources in the same region, including 1014 newly discovered X-ray sources. About 200 sources in Stiele et al. (2011)'s catalogue are rejected due to their low detection likelihood (e.g.,  $< 30$ ). The archival Chandra data of M31 has a better angular resolution, but covers a small portion of the disk. We also include the information of the cross-matched Chandra sources (from the Chandra Source Catalog Release 2.0; Evans & Civano 2018) in our catalogue for comparison.

For each source, the reported parameters can be classified into three categories. We first summarize the basic detection information, including the position, the detection likelihood, and the involved observations where the source is detected. The second is the physical parameters of the source, count rate, flux, hardness ratio, extent etc. These parameters are not only reported for combined result from all involved exposures, but also for individual observation, instruments (all-EPIC, pn, MOS1,



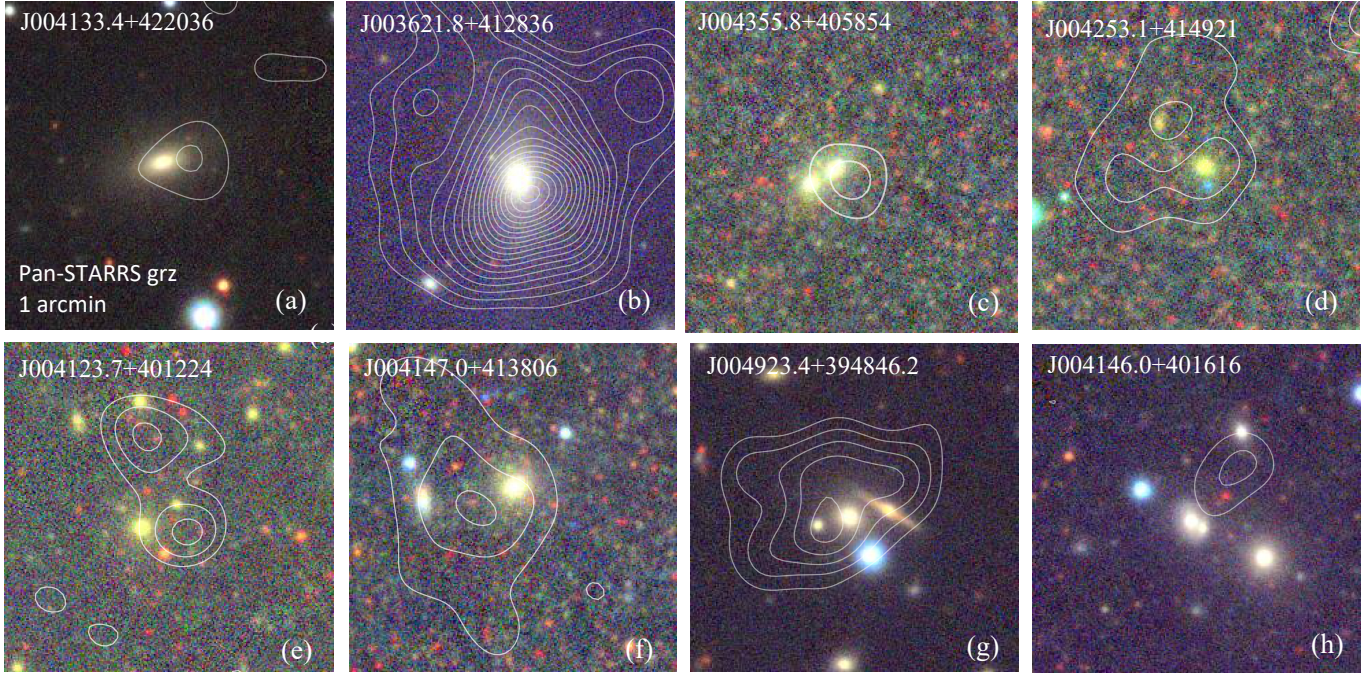


**Figure 9.** The X-ray contour and optical image of 8 extended galaxies. The contours are the 2 sigma (background uncertainty) and above of the 0.5-4.5 keV X-ray count rate images smoothed with 5 arcsec Gaussian kernel. The  $1 \times 1$  arcmin<sup>2</sup> optical images are from Pan-STARRS g, r and z band.

and MOS2), and energy bands (0.2-12.0 keV, 0.2-0.5 keV, 0.5-1.0 keV, 1.0-2.0 keV, 2.0-4.5 keV, and 4.5-12.0 keV). The last is the classification, we list our preferred identification or classification of the source based on either the multi-wavelength cross-identification (§3.2) or the brief multi-color classification (§3.3). We describe the catalogue of the source parameters in Appendix D. A machine-readable format of the table is provided online only.

Results of the classification in our X-ray source catalogue are also summarized in Table 2. Based on the multi-wavelength cross-identifications, in our X-ray source catalogue, we identify 352 single stars in the foreground (fg stars; all regarded as firmly identified), 35 firmly identified GICs and 31 SNRs (27 firmly identified, 4 as candidates) associated with M 31, as well as 567 AGNs (62 firmly identified, 505 as candidates), 62 galaxies (59 firmly identified, 3 as candidates), and 6 GCLs (1 firmly identified, 5 as candidates) in the background. We uniquely classify 236 fg star and 17 SSS candidates based on their X-ray colors. Since the LMXBs, HMXBs, and AGNs are not explicitly separated just based on their X-ray and optical colors, we often give them a preferred but not confirmed classification based on multiple criteria (based on the X-ray colors, X-ray-to-optical colors, and X-ray variability). The exceptions are some highly variable X-ray sources which are regarded as firmly identified XRBs. 83 of them are identified as LMXBs, and 1

of them is taken as HMXBs. The remaining 3116 X-ray sources either have too low S/N to calculate their X-ray colors or have not unique classification, so are regarded as unclassified.

We do not perform standard astrometry correction to individual observations before conducting source detection. This is partially because the astrometry correction, typically calculated based on cross-matching the X-ray and optical sources, could be largely uncertain, especially in the halo of M 31 where only a few sources can be identified in optical. Instead, we directly apply the astrometry correction result for each observations after detecting the sources, using the suggested offset values from the 4XMM-DR12s catalogue (Traulsen et al. 2020). For sources detected in overlapping observations, we weight the offset of different observations by the number of counts of the detected sources in the corresponding observations. We also list the updated source position (`ast_RA` and `ast_DEC`) considering the astrometry correction in the catalogue. Besides the original identification and classification result (`type`), the sources with an updated astrometry correction has a slightly different multi-wavelength cross-matching result. We also list this updated identification and classification result (`ast_type`) in the catalogue for reference, but caution that this is based on a simple geometric correction, without updating the source detection parameters.

We publish the full source catalogue with the X-ray/multi-wavelength properties of the sources and their classifications as an online only table (§D, §E, and Table A.2). This source catalogue is unique for the study of the X-ray source populations, as well as quantitatively estimating the contribution of X-ray sources in the unresolved X-ray emissions of an external galaxy. These topics will be discussed in the follow-up papers. We also summarize our X-ray source classification criteria in Table 2, which are potentially applicable to other galaxies.

#### ACKNOWLEDGEMENTS

The authors would like to thank Prof. Junjie Mao (Tsinghua University) and Prof. B. Luo (Nanjing University) for helpful discussions. This work was supported in part by the Ministry of Science and Technology of China through Grant 2018YFA0404502 and the National Natural Science Foundation of China through Grants E3GJ251110 and 11821303. RH acknowledges support from the China Scholarship Council. GP acknowledges funding from the European Research Council (ERC) under the European Union’s Horizon 2020 research and innovation programme (grant agreement No 865637) and from ”Bando per il Finanziamento della Ricerca Fondamentale 2022 dell’Istituto Nazionale di Astrofisica (INAF): Canale: GO Large program”

This publication makes use of data products from the Wide-field Infrared Survey Explorer, which is a joint project of the University of California, Los Angeles, and the Jet Propulsion Laboratory/California Institute of Technology, funded by the National Aeronautics and Space Administration. This work has made use of data from the European Space Agency (ESA) mission *Gaia* ([www.cosmos.esa.int/gaia](http://www.cosmos.esa.int/gaia)), processed by the *Gaia* Data Processing and Analysis Consortium (DPAC, [www.cosmos.esa.int/web/gaia/dpac/consortium](http://www.cosmos.esa.int/web/gaia/dpac/consortium)). Funding for the DPAC has been provided by national institutions, in particular the institutions participating in the *Gaia* Multilateral Agreement. This research has made use of the VizieR catalog access tool, CDS, Strasbourg, France (DOI : 10.26093/cds/vizieR). The original description of the VizieR service was published in 2000, A&AS 143, 23

Data Availability: The X-ray source catalogue is published online in machine-readable format. The original *XMM-Newton* data used in the presented paper is available on the *XMM-Newton* data archive. The reduced data could be shared by reasonable request to the corresponding author.

#### REFERENCES

- Bahramian, A., Strader, J., Miller-Jones, J. C. A., et al. 2020, ApJ, 901, 57, doi: [10.3847/1538-4357/aba51d](https://doi.org/10.3847/1538-4357/aba51d)
- Barmby, P., Ashby, M. L. N., Bianchi, L., et al. 2006, ApJL, 650, L45, doi: [10.1086/508626](https://doi.org/10.1086/508626)
- Bilicki, M., Jarrett, T. H., Peacock, J. A., Cluver, M. E., & Steward, L. 2014, ApJS, 210, 9, doi: [10.1088/0067-0049/210/1/9](https://doi.org/10.1088/0067-0049/210/1/9)
- Binder, B., Williams, B. F., Eracleous, M., et al. 2015, AJ, 150, 94, doi: [10.1088/0004-6256/150/3/94](https://doi.org/10.1088/0004-6256/150/3/94)
- Blair, W. P., Winkler, P. F., & Long, K. S. 2012, ApJS, 203, 8, doi: [10.1088/0067-0049/203/1/8](https://doi.org/10.1088/0067-0049/203/1/8)
- Blair, W. P., Winkler, P. F., Long, K. S., et al. 2015, ApJ, 800, 118, doi: [10.1088/0004-637X/800/2/118](https://doi.org/10.1088/0004-637X/800/2/118)
- Bogdán, Á., & Gilfanov, M. 2008, MNRAS, 388, 56, doi: [10.1111/j.1365-2966.2008.13391.x](https://doi.org/10.1111/j.1365-2966.2008.13391.x)
- . 2010, MNRAS, 405, 209, doi: [10.1111/j.1365-2966.2010.16476.x](https://doi.org/10.1111/j.1365-2966.2010.16476.x)
- Bozzetto, L. M., Filipović, M. D., Vukotić, B., et al. 2017, ApJS, 230, 2, doi: [10.3847/1538-4365/aa653c](https://doi.org/10.3847/1538-4365/aa653c)
- Brightman, M., Silverman, J. D., Mainieri, V., et al. 2013, MNRAS, 433, 2485, doi: [10.1093/mnras/stt920](https://doi.org/10.1093/mnras/stt920)
- Buchner, J., Salvato, M., Budavári, T., & Fotopoulou, S. 2021, nway: Bayesian cross-matching of astronomical catalogs, Astrophysics Source Code Library, record ascl:2102.014. <http://ascl.net/2102.014>
- Caldwell, N., Harding, P., Morrison, H., et al. 2009, AJ, 137, 94, doi: [10.1088/0004-6256/137/1/94](https://doi.org/10.1088/0004-6256/137/1/94)
- Cash, W. 1979, ApJ, 228, 939, doi: [10.1086/156922](https://doi.org/10.1086/156922)
- Chambers, K. C., Magnier, E. A., Metcalfe, N., et al. 2016, arXiv e-prints, arXiv:1612.05560, doi: [10.48550/arXiv.1612.05560](https://doi.org/10.48550/arXiv.1612.05560)
- Chen, C. T. J., Brandt, W. N., Luo, B., et al. 2018, MNRAS, 478, 2132, doi: [10.1093/mnras/sty1036](https://doi.org/10.1093/mnras/sty1036)
- Cutri, R. M., Wright, E. L., Conrow, T., et al. 2021, VizieR Online Data Catalog, II/328
- Dalcanton, J. J., Williams, B. F., Lang, D., et al. 2012, ApJS, 200, 18, doi: [10.1088/0067-0049/200/2/18](https://doi.org/10.1088/0067-0049/200/2/18)
- Delchambre, L., Bailer-Jones, C. A. L., Bellas-Velidis, I., et al. 2022, arXiv e-prints, arXiv:2206.06710, doi: [10.48550/arXiv.2206.06710](https://doi.org/10.48550/arXiv.2206.06710)
- Di Stefano, R., Kong, A. K. H., Greiner, J., et al. 2004, ApJ, 610, 247, doi: [10.1086/421696](https://doi.org/10.1086/421696)



- Esposito, P., Motta, S. E., Pintore, F., Zampieri, L., & Tomasella, L. 2013, *MNRAS*, 428, 2480, doi: [10.1093/mnras/sts248](https://doi.org/10.1093/mnras/sts248)
- Evans, I. N., & Civano, F. 2018, *Astronomy and Geophysics*, 59, 2.17, doi: [10.1093/astrogeo/aty079](https://doi.org/10.1093/astrogeo/aty079)
- Fabbiano, G. 2006, *ARA&A*, 44, 323, doi: [10.1146/annurev.astro.44.051905.092519](https://doi.org/10.1146/annurev.astro.44.051905.092519)
- Flesch, E. W. 2015, *PASA*, 32, e010, doi: [10.1017/pasa.2015.10](https://doi.org/10.1017/pasa.2015.10)
- Gaia Collaboration. 2022, *VizieR Online Data Catalog*, I/355
- Gaia Collaboration, Prusti, T., de Bruijne, J. H. J., et al. 2016, *A&A*, 595, A1, doi: [10.1051/0004-6361/201629272](https://doi.org/10.1051/0004-6361/201629272)
- Gaia Collaboration, Brown, A. G. A., Vallenari, A., et al. 2021, *A&A*, 649, A1, doi: [10.1051/0004-6361/202039657](https://doi.org/10.1051/0004-6361/202039657)
- Galleti, S., Bellazzini, M., Federici, L., Buzzoni, A., & Fusi Pecci, F. 2007, *A&A*, 471, 127, doi: [10.1051/0004-6361:20077788](https://doi.org/10.1051/0004-6361:20077788)
- Galleti, S., Federici, L., Bellazzini, M., Fusi Pecci, F., & Macrina, S. 2004, *A&A*, 416, 917, doi: [10.1051/0004-6361:20035632](https://doi.org/10.1051/0004-6361:20035632)
- Galleti, S., Federici, L., Bellazzini, M., et al. 2014, *VizieR Online Data Catalog*, V/143
- Gilfanov, M. 2004, *MNRAS*, 349, 146, doi: [10.1111/j.1365-2966.2004.07473.x](https://doi.org/10.1111/j.1365-2966.2004.07473.x)
- Green, D. A. 2019, *Journal of Astrophysics and Astronomy*, 40, 36, doi: [10.1007/s12036-019-9601-6](https://doi.org/10.1007/s12036-019-9601-6)
- Greiner, J. 2000, *NewA*, 5, 137, doi: [10.1016/S1384-1076\(00\)00018-X](https://doi.org/10.1016/S1384-1076(00)00018-X)
- Güdel, M. 2004, *A&A Rv*, 12, 71, doi: [10.1007/s00159-004-0023-2](https://doi.org/10.1007/s00159-004-0023-2)
- Heinke, C. O., Grindlay, J. E., Edmonds, P. D., et al. 2005, *ApJ*, 625, 796, doi: [10.1086/429899](https://doi.org/10.1086/429899)
- Henze, M., Pietsch, W., & Haberl, F. 2012, *The Astronomer's Telegram*, 3921, 1
- Henze, M., Pietsch, W., Haberl, F., & Greiner, J. 2009, *The Astronomer's Telegram*, 2356, 1
- HI4PI Collaboration, Ben Bekhti, N., Flöer, L., et al. 2016, *A&A*, 594, A116, doi: [10.1051/0004-6361/201629178](https://doi.org/10.1051/0004-6361/201629178)
- Irwin, J. A., Athey, A. E., & Bregman, J. N. 2003, *ApJ*, 587, 356, doi: [10.1086/368179](https://doi.org/10.1086/368179)
- Irwin, J. A., Sarazin, C. L., & Bregman, J. N. 2002, *ApJ*, 570, 152, doi: [10.1086/339734](https://doi.org/10.1086/339734)
- Jennings, Z. G., Williams, B. F., Murphy, J. W., et al. 2014, *ApJ*, 795, 170, doi: [10.1088/0004-637X/795/2/170](https://doi.org/10.1088/0004-637X/795/2/170)
- Jonker, P. G., & Nelemans, G. 2004, *MNRAS*, 354, 355, doi: [10.1111/j.1365-2966.2004.08193.x](https://doi.org/10.1111/j.1365-2966.2004.08193.x)
- Kaur, A., Henze, M., Haberl, F., et al. 2012, *A&A*, 538, A49, doi: [10.1051/0004-6361/201118025](https://doi.org/10.1051/0004-6361/201118025)
- Kavanagh, P. J., Sasaki, M., Breitschwerdt, D., et al. 2020, *A&A*, 637, A12, doi: [10.1051/0004-6361/201937008](https://doi.org/10.1051/0004-6361/201937008)
- Kim, D.-W., & Fabbiano, G. 2004, *ApJ*, 611, 846, doi: [10.1086/422210](https://doi.org/10.1086/422210)
- Kim, D. W., Fabbiano, G., Brassington, N. J., et al. 2009, *ApJ*, 703, 829, doi: [10.1088/0004-637X/703/1/829](https://doi.org/10.1088/0004-637X/703/1/829)
- Kong, A. K. H., DiStefano, R., Garcia, M. R., & Greiner, J. 2003, *ApJ*, 585, 298, doi: [10.1086/345947](https://doi.org/10.1086/345947)
- Kotov, O., Trudolyubov, S., & Vestrand, W. T. 2006, *ApJ*, 641, 756, doi: [10.1086/500630](https://doi.org/10.1086/500630)
- Lazzarini, M., Williams, B. F., Durbin, M., et al. 2021, *ApJ*, 906, 120, doi: [10.3847/1538-4357/abccca](https://doi.org/10.3847/1538-4357/abccca)
- Lee, J. H., & Lee, M. G. 2014, *ApJ*, 786, 130, doi: [10.1088/0004-637X/786/2/130](https://doi.org/10.1088/0004-637X/786/2/130)
- Lehmer, B. D., Alexander, D. M., Bauer, F. E., et al. 2010, *ApJ*, 724, 559, doi: [10.1088/0004-637X/724/1/559](https://doi.org/10.1088/0004-637X/724/1/559)
- Li, J.-T., Bregman, J. N., Wang, Q. D., Crain, R. A., & Anderson, M. E. 2016, *ApJ*, 830, 134, doi: [10.3847/0004-637X/830/2/134](https://doi.org/10.3847/0004-637X/830/2/134)
- . 2018, *ApJL*, 855, L24, doi: [10.3847/2041-8213/aab2af](https://doi.org/10.3847/2041-8213/aab2af)
- Li, J.-T., Bregman, J. N., Wang, Q. D., et al. 2017, *ApJS*, 233, 20, doi: [10.3847/1538-4365/aa96fc](https://doi.org/10.3847/1538-4365/aa96fc)
- Li, J.-T., Li, Z., Wang, Q. D., Irwin, J. A., & Rossa, J. 2008, *MNRAS*, 390, 59, doi: [10.1111/j.1365-2966.2008.13749.x](https://doi.org/10.1111/j.1365-2966.2008.13749.x)
- Li, J.-T., Wang, F., Yang, J., et al. 2021a, *MNRAS*, 504, 2767, doi: [10.1093/mnras/stab1042](https://doi.org/10.1093/mnras/stab1042)
- Li, J.-T., & Wang, Q. D. 2013a, *MNRAS*, 428, 2085, doi: [10.1093/mnras/sts183](https://doi.org/10.1093/mnras/sts183)
- . 2013b, *MNRAS*, 435, 3071, doi: [10.1093/mnras/stt1501](https://doi.org/10.1093/mnras/stt1501)
- Li, S., Riess, A. G., Busch, M. P., et al. 2021b, *ApJ*, 920, 84, doi: [10.3847/1538-4357/ac1597](https://doi.org/10.3847/1538-4357/ac1597)
- Li, Z., & Wang, Q. D. 2007, *ApJL*, 668, L39, doi: [10.1086/522674](https://doi.org/10.1086/522674)
- Liu, Q. Z., van Paradijs, J., & van den Heuvel, E. P. J. 2007, *A&A*, 469, 807, doi: [10.1051/0004-6361:20077303](https://doi.org/10.1051/0004-6361:20077303)
- Long, K. S., Blair, W. P., Winkler, P. F., et al. 2010, *ApJS*, 187, 495, doi: [10.1088/0067-0049/187/2/495](https://doi.org/10.1088/0067-0049/187/2/495)
- Lyke, B. W., Higley, A. N., McLane, J. N., et al. 2020, *ApJS*, 250, 8, doi: [10.3847/1538-4365/aba623](https://doi.org/10.3847/1538-4365/aba623)
- Maggi, P., Haberl, F., Kavanagh, P. J., et al. 2016, *A&A*, 585, A162, doi: [10.1051/0004-6361/201526932](https://doi.org/10.1051/0004-6361/201526932)
- Maggi, P., Filipović, M. D., Vukotić, B., et al. 2019, *A&A*, 631, A127, doi: [10.1051/0004-6361/201936583](https://doi.org/10.1051/0004-6361/201936583)
- Massey, P., Olsen, K. A. G., Hodge, P. W., et al. 2006, *AJ*, 131, 2478, doi: [10.1086/503256](https://doi.org/10.1086/503256)
- Miller, J. M., Fabian, A. C., & Miller, M. C. 2004, *ApJL*, 614, L117, doi: [10.1086/425316](https://doi.org/10.1086/425316)
- Mineo, S., Gilfanov, M., & Sunyaev, R. 2012, *MNRAS*, 419, 2095, doi: [10.1111/j.1365-2966.2011.19862.x](https://doi.org/10.1111/j.1365-2966.2011.19862.x)

- Mukai, K. 2017, *PASP*, 129, 062001, doi: [10.1088/1538-3873/aa6736](https://doi.org/10.1088/1538-3873/aa6736)
- Ni, Q., Brandt, W. N., Chen, C.-T., et al. 2021, *ApJS*, 256, 21, doi: [10.3847/1538-4365/ac0dc6](https://doi.org/10.3847/1538-4365/ac0dc6)
- Pietsch, W., Fliri, J., Freyberg, M. J., et al. 2005a, *A&A*, 442, 879, doi: [10.1051/0004-6361:20053127](https://doi.org/10.1051/0004-6361:20053127)
- Pietsch, W., Freyberg, M., & Haberl, F. 2005b, *A&A*, 434, 483, doi: [10.1051/0004-6361:20041990](https://doi.org/10.1051/0004-6361:20041990)
- Remillard, R. A., & McClintock, J. E. 2006, *ARA&A*, 44, 49, doi: [10.1146/annurev.astro.44.051905.092532](https://doi.org/10.1146/annurev.astro.44.051905.092532)
- Revnivtsev, M., Churazov, E., Sazonov, S., Forman, W., & Jones, C. 2008, *A&A*, 490, 37, doi: [10.1051/0004-6361:200809889](https://doi.org/10.1051/0004-6361:200809889)
- Revnivtsev, M., Sazonov, S., Churazov, E., et al. 2009, *Nature*, 458, 1142, doi: [10.1038/nature07946](https://doi.org/10.1038/nature07946)
- Revnivtsev, M., Sazonov, S., Forman, W., Churazov, E., & Sunyaev, R. 2011, *MNRAS*, 414, 495, doi: [10.1111/j.1365-2966.2011.18411.x](https://doi.org/10.1111/j.1365-2966.2011.18411.x)
- Revnivtsev, M., Vikhlinin, A., & Sazonov, S. 2007, *A&A*, 473, 857, doi: [10.1051/0004-6361:20066850](https://doi.org/10.1051/0004-6361:20066850)
- Rosner, R., Golub, L., & Vaiana, G. S. 1985, *ARA&A*, 23, 413, doi: [10.1146/annurev.aa.23.090185.002213](https://doi.org/10.1146/annurev.aa.23.090185.002213)
- Salvato, M., Buchner, J., Budavári, T., et al. 2018, *MNRAS*, 473, 4937, doi: [10.1093/mnras/stx2651](https://doi.org/10.1093/mnras/stx2651)
- Sana, H., Rauw, G., Nazé, Y., Gosset, E., & Vreux, J. M. 2006, *MNRAS*, 372, 661, doi: [10.1111/j.1365-2966.2006.10847.x](https://doi.org/10.1111/j.1365-2966.2006.10847.x)
- Sasaki, M., Pietsch, W., Haberl, F., et al. 2012, *A&A*, 544, A144, doi: [10.1051/0004-6361/201219025](https://doi.org/10.1051/0004-6361/201219025)
- Sasaki, M., Haberl, F., Henze, M., et al. 2018, *A&A*, 620, A28, doi: [10.1051/0004-6361/201833588](https://doi.org/10.1051/0004-6361/201833588)
- Sazonov, S., Revnivtsev, M., Gilfanov, M., Churazov, E., & Sunyaev, R. 2006, *A&A*, 450, 117, doi: [10.1051/0004-6361:20054297](https://doi.org/10.1051/0004-6361:20054297)
- Schmitt, J. H. M. M., Fleming, T. A., & Giampapa, M. S. 1995, *ApJ*, 450, 392, doi: [10.1086/176149](https://doi.org/10.1086/176149)
- Shaw Greening, L., Barnard, R., Kolb, U., Tonkin, C., & Osborne, J. P. 2009, *A&A*, 495, 733, doi: [10.1051/0004-6361/200809864](https://doi.org/10.1051/0004-6361/200809864)
- Singh, G., & Pandey, J. C. 2022, *ApJ*, 934, 20, doi: [10.3847/1538-4357/ac7716](https://doi.org/10.3847/1538-4357/ac7716)
- Stiele, H., Pietsch, W., Haberl, F., & Freyberg, M. 2008, *A&A*, 480, 599, doi: [10.1051/0004-6361:20078858](https://doi.org/10.1051/0004-6361:20078858)
- Stiele, H., Pietsch, W., Haberl, F., et al. 2011, *A&A*, 534, A55, doi: [10.1051/0004-6361/201015270](https://doi.org/10.1051/0004-6361/201015270)
- Sun, M., Voit, G. M., Donahue, M., et al. 2009, *ApJ*, 693, 1142, doi: [10.1088/0004-637X/693/2/1142](https://doi.org/10.1088/0004-637X/693/2/1142)
- Supper, R., Hasinger, G., Lewin, W. H. G., et al. 2001, *A&A*, 373, 63, doi: [10.1051/0004-6361:20010495](https://doi.org/10.1051/0004-6361:20010495)
- Supper, R., Hasinger, G., Pietsch, W., et al. 1997, *A&A*, 317, 328
- Tamm, A., Tempel, E., Tenjes, P., Tihhonova, O., & Tuvikene, T. 2012, *A&A*, 546, A4, doi: [10.1051/0004-6361/201220065](https://doi.org/10.1051/0004-6361/201220065)
- Traulsen, I., Schwöpe, A. D., Lamer, G., et al. 2019, *A&A*, 624, A77, doi: [10.1051/0004-6361/201833938](https://doi.org/10.1051/0004-6361/201833938)
- . 2020, *A&A*, 641, A137, doi: [10.1051/0004-6361/202037706](https://doi.org/10.1051/0004-6361/202037706)
- . 2022, *VizieR Online Data Catalog*, IX/66
- Trinchieri, G., & Fabbiano, G. 1991, *ApJ*, 382, 82, doi: [10.1086/170696](https://doi.org/10.1086/170696)
- van Speybroeck, L., Epstein, A., Forman, W., et al. 1979, *ApJL*, 234, L45, doi: [10.1086/183106](https://doi.org/10.1086/183106)
- Voss, R., & Gilfanov, M. 2007, *A&A*, 468, 49, doi: [10.1051/0004-6361:20066614](https://doi.org/10.1051/0004-6361:20066614)
- Watson, M. G., Schröder, A. C., Fyfe, D., et al. 2009, *Astronomy & Astrophysics*, 493, 339
- Webb, N. A., Coriat, M., Traulsen, I., et al. 2020, *A&A*, 641, A136, doi: [10.1051/0004-6361/201937353](https://doi.org/10.1051/0004-6361/201937353)
- Wenger, M., Ochsenein, F., Egret, D., et al. 2000, *A&AS*, 143, 9, doi: [10.1051/aas:2000332](https://doi.org/10.1051/aas:2000332)
- White, R. L., Long, K. S., Becker, R. H., et al. 2019, *ApJS*, 241, 37, doi: [10.3847/1538-4365/ab0e89](https://doi.org/10.3847/1538-4365/ab0e89)
- Williams, B. F., Lang, D., Dalcanton, J. J., et al. 2014, *ApJS*, 215, 9, doi: [10.1088/0067-0049/215/1/9](https://doi.org/10.1088/0067-0049/215/1/9)
- Williams, B. F., Lazzarini, M., Plucinsky, P. P., et al. 2018, *ApJS*, 239, 13, doi: [10.3847/1538-4365/aae37d](https://doi.org/10.3847/1538-4365/aae37d)
- Zhang, Z., Gilfanov, M., Voss, R., et al. 2011, *A&A*, 533, A33, doi: [10.1051/0004-6361/201116936](https://doi.org/10.1051/0004-6361/201116936)
- Zhao, J., & Heinke, C. O. 2022, *MNRAS*, 511, 5964, doi: [10.1093/mnras/stac442](https://doi.org/10.1093/mnras/stac442)
- Zhu, Z., Li, Z., & Morris, M. R. 2018, *ApJS*, 235, 26, doi: [10.3847/1538-4365/aab14f](https://doi.org/10.3847/1538-4365/aab14f)
- Zuo, Z.-Y., Li, X.-D., & Liu, X.-W. 2008, *MNRAS*, 387, 121, doi: [10.1111/j.1365-2966.2008.12974.x](https://doi.org/10.1111/j.1365-2966.2008.12974.x)

## APPENDIX

## A. XMM-NEWTON DATA USED IN THE NEW-ANGELS PROGRAM

**Table A.1.** The *XMM-Newton* observations used in the New-ANGELS program. The total good time interval (GTI) of the mos1, mos2 and PN cameras are in unit of ks. M and T1 in the filter columns refer to the median and thin1 filter.

Begin of Table											
ObsID	RA	DEC	Start Date	PI	$t_{M1}$ (GTI)	$t_{M2}$ (GTI)	$t_{PN}$ (GTI)	filter <sub>M1</sub>	filter <sub>M2</sub>	filter <sub>PN</sub>	
0109270101	00 42 42.9	+41 15 46.0	2001-06-29	Mason	50.8 (28.4)	50.8 (30.8)	45.5 (25.1)	M	M	M	
0109270301	00 45 20.0	+41 56 09.0	2002-01-26	Mason	55.6 (26.6)	55.9 (26.9)	27.5 (25.4)	M	M	M	
0109270401	00 46 38.0	+42 16 20.0	2002-06-29	Mason	53.3 (48.9)	53.9 (50.1)	91.6 (64.2)	M	M	M	
0109270701	00 44 00.9	+41 35 57.0	2002-01-05	Mason	57.4 (56.8)	57.4 (57.0)	54.9 (54.5)	M	M	M	
0112570101	00 42 42.9	+41 15 46.0	2002-01-06	Watson	62.5 (59.6)	63.7 (59.9)	53.2 (50.1)	T1	T1	T1	
0112570201	00 41 24.9	+40 55 35.0	2002-01-12	Watson	66.5 (55.5)	66.5 (55.3)	59.6 (51.3)	T1	T1	T1	
0112570301	00 40 06.0	+40 35 24.0	2002-01-24	Watson	53.1 (28.5)	53.3 (30.3)	45.4 (21.5)	T1	T1	T1	
0112570401	00 42 42.9	+41 15 46.0	2000-06-25	Watson	30.0 (29.9)	30.0 (29.5)	26.3 (26.1)	M	M	M	
0151580201	00 43 11.9	+39 47 60.0	2003-02-03	Di Stefano		flared					
0151580301	00 45 59.0	+40 42 36.0	2003-02-03	Di Stefano		flared					
0151580401	00 46 06.9	+41 20 58.0	2003-02-06	Di Stefano	13.2 (12.8)	13.2 (12.8)	11.5 (11.1)	M	M	M	
0151581201	00 43 11.9	+39 47 60.0	2003-07-01	Di Stefano		flared					
0151581301	00 45 59.0	+40 42 36.0	2003-07-01	Di Stefano	6.4(2.2)	6.4(2.3)		M	M		
0202230301	00 42 38.5	+41 16 03.8	2004-07-17	Barnard		flared					
0204790401	00 40 22.2	+41 41 09.0	2004-01-02	Di Stefano		flared					
0300910201	00 41 53.3	+40 21 18.0	2005-08-01	Piconcelli		flared					
0402560101	00 38 52.8	+40 15 00.0	2006-06-28	Pietsch	42.1 (6.1)	9.1 (3.6)	42.1 (6.7)	M	M	T1	
0402560201	00 43 28.8	+40 55 12.0	2006-06-30	Pietsch		flared					
0402560301	00 40 43.2	+41 17 60.0	2006-07-01	Pietsch	61.4 (48.0)	61.4 (49.4)	57.6 (39.0)	M	M	T1	
0402560401	00 42 16.8	+40 37 12.0	2006-07-08	Pietsch		flared					
0402560501	00 39 40.7	+40 58 48.0	2006-07-20	Pietsch	58.7 (54.8)	58.7 (56.3)	47.6 (28.6)	M	M	T1	
0402560601	00 40 45.6	+40 21 05.1	2006-07-28	Pietsch	49.4 (32.4)	49.2 (32.2)	42.6 (25.1)	M	M	T1	
0402560701	00 39 02.4	+40 37 48.0	2006-07-23	Pietsch	61.1 (26.0)	61.7 (30.7)	51.2 (18.3)	M	M	T1	
0402560801	00 40 06.0	+40 35 24.0	2006-12-25	Pietsch	52.1 (49.8)	52.1 (49.0)	50.8 (44.1)	M	M	T1	
0402560901	00 41 52.7	+41 36 36.0	2006-12-26	Pietsch	49.0 (45.6)	49.0 (45.3)	44.6 (40.8)	M	M	T1	
0402561001	00 44 38.4	+41 12 01.0	2006-12-30	Pietsch	54.8 (52.0)	54.7 (53.3)	45.8 (42.2)	M	M	T1	
0402561101	00 43 09.6	+41 55 12.0	2007-01-01	Pietsch	57.8 (47.7)	57.9 (47.1)	57.6 (42.5)	M	M	T1	
0402561201	00 45 43.1	+41 31 48.0	2007-01-02	Pietsch	54.4 (41.4)	54.4 (40.7)	53.0 (35.7)	M	M	T1	
0402561301	00 44 45.5	+42 09 36.0	2007-01-03	Pietsch	54.3 (36.4)	54.3 (36.0)	40.3 (29.6)	M	M	T1	
0402561401	00 46 38.4	+41 53 60.0	2007-01-04	Pietsch	52.4 (46.1)	52.4 (46.5)	51.0 (43.4)	M	M	T1	
0402561501	00 45 20.0	+41 56 09.0	2007-01-05	Pietsch	45.4 (43.8)	45.4 (43.8)	43.0 (37.9)	M	M	T1	
0404060201	00 45 19.5	+40 57 47.0	2006-07-03	Bregman	35.3 (21.1)	35.3 (22.3)	33.6 (16.1)	T1	T1	T1	
0405320501	00 42 44.3	+41 16 09.4	2006-07-02	Pietsch	21.4 (13.4)	21.7 (15.1)	13.3 (9.5)	M	M	T1	
0405320601	00 42 44.3	+41 16 09.4	2006-08-09	Pietsch		flared					
0405320801	00 42 44.3	+41 16 09.4	2007-01-16	Pietsch		flared					

Continuation of Table A.1

ObsID	RA	DEC	Start Date	PI	$t_{M1}^0$ (GTI)	$t_{M2}$ (GTI)	$t_{PN}$ (GTI)	filter <sub>M1</sub>	filter <sub>M2</sub>	filter <sub>PN</sub>
0405320901	00 42 44.3	+41 16 09.4	2007-02-05	Pietsch	16.4 (16.0)	16.6 (16.3)	15.0 (13.2)			
0410582001	00 40 59.1	+41 15 51.2	2007-07-25	Schartel	15.9 (14.9)	15.9 (15.5)	13.4 (10.5)	M	M	T1
0505720201	00 42 44.3	+41 16 09.4	2007-12-29	Pietsch	27.2 (26.9)	27.2 (27.1)	25.7 (25.6)	M	M	T1
0505720301	00 42 44.3	+41 16 09.4	2008-01-08	Pietsch	26.9 (26.4)	26.9 (26.3)	24.4 (22.8)	M	M	T1
0505720401	00 42 44.3	+41 16 09.4	2008-01-18	Pietsch	22.4 (21.6)	22.4 (21.5)	20.8 (17.2)	M	M	T1
0505720501	00 42 44.3	+41 16 09.4	2008-01-27	Pietsch	21.5 (14.2)	21.5 (15.0)	15.0 (7.8)	M	M	T1
0505720601	00 42 44.3	+41 16 09.4	2008-02-07	Pietsch		flared				
0505760101	00 38 52.8	+40 15 00.0	2007-07-24	Pietsch	35.5 (27.6)	55.7 (29.7)	34.8 (17.8)	M	M	T1
0505760201	00 43 28.8	+40 55 12.0	2007-07-22	Pietsch	57.5 (42.4)	57.5 (47.1)	34.6 (23.8)	M	M	T1
0505760301	00 42 16.8	+40 37 12.0	2007-12-28	Pietsch	44.2 (42.7)	44.4 (44.0)	40.1 (39.5)	M	M	T1
0505760401	00 40 45.6	+40 21 05.1	2007-12-25	Pietsch	28.6 (28.5)	28.6 (28.4)	27.1 (26.3)	M	M	T1
0505760501	00 39 02.4	+40 37 48.0	2007-12-31	Pietsch	38.6 (34.5)	38.6 (35.1)	37.0 (25.8)	M	M	T1
0505900101	00 38 19.5	+41 47 15.0	2007-07-21	Tanvir		flared				
0505900301	00 38 04.5	+40 44 39.0	2007-12-27	Tanvir		flared				
0505900801	00 38 04.5	+40 44 39.0	2008-02-09	Tanvir		flared				
0511380101	00 38 52.8	+40 15 00.0	2008-01-02	Pietsch	45.6 (45.4)	45.6 (45.4)	44.0 (41.4)	M	M	T1
0511380201	00 43 28.8	+40 55 12.0	2008-01-05	Pietsch		flared				
0511380301	00 39 40.7	+40 58 48.0	2008-01-06	Pietsch	35.4 (33.1)	35.4 (33.0)	33.9 (27.4)	M	M	T1
0511380601	00 43 28.8	+40 55 12.0	2008-02-09	Pietsch		flared				
0551690201	00 42 44.3	+41 16 09.4	2008-12-30	Pietsch		flared				
0551690301	00 42 44.3	+41 16 09.4	2009-01-09	Pietsch	21.6 (20.8)	21.6 (20.6)	20.0 (18.3)	M	M	T1
0551690401	00 42 44.3	+41 16 09.4	2009-01-15	Pietsch	17.1 (5.3)	11.4 (5.1)	9.4 (3.5)	M	M	T1
0551690501	00 42 44.3	+41 16 09.4	2009-01-27	Pietsch		flared				
0551690601	00 42 44.3	+41 16 09.4	2009-02-04	Pietsch		flared				
0560180101	00 43 19.9	+41 13 46.6	2008-07-18	Schartel	21.1 (9.2)	19.9 (8.8)	16.5 (4.4)	M	M	T1
0600660201	00 42 44.3	+41 16 09.4	2009-12-28	Pietsch	18.5 (18.1)	18.5 (17.8)	16.9 (16.1)			
0600660301	00 42 44.3	+41 16 09.4	2010-01-07	Pietsch	17.0 (16.9)	17.0 (16.9)	15.4 (14.8)			
0600660401	00 42 44.3	+41 16 09.4	2010-01-15	Pietsch	16.8 (16.7)	16.5 (16.4)	12.7 (7.7)			
0600660501	00 42 44.3	+41 16 09.4	2010-01-25	Pietsch	19.3 (13.7)	19.4 (16.1)	17.8 (17.8)			
0600660601	00 42 44.3	+41 16 09.4	2010-02-02	Pietsch	17.0 (16.0)	17.0 (16.2)	15.4 (10.2)			
0650560201	00 42 44.3	+41 16 09.4	2010-12-26	Pietsch		flared				
0650560301	00 42 44.3	+41 16 09.4	2011-01-04	Pietsch	33.1 (28.6)	33.1 (30.9)	30.6 (17.9)	M	M	T1
0650560401	00 42 44.3	+41 16 09.4	2011-01-14	Pietsch	21.8 (13.1)	22.1 (15.4)	21.5 (10.1)	M	M	T1
0650560501	00 42 44.3	+41 16 09.4	2011-01-25	Pietsch	23.6 (22.8)	23.6 (22.8)	9.2 (5.5)	M	M	T1
0650560601	00 42 44.3	+41 16 09.4	2011-02-03	Pietsch	23.3 (22.0)	23.3 (22.5)	18.7 (11.0)	M	M	T1
0652500101	00 46 55.0	+40 31 00.0	2011-02-01	Di Stefano		flared				
0652500201	00 49 05.0	+40 17 32.0	2011-02-01	Di Stefano	21.6 (12.1)	21.6 (12.2)	20.0 (8.3)	T1	T1	T1
0652500301	00 53 27.9	+39 49 46.0	2011-02-03	Di Stefano		flared				
0655620301	00 43 45.5	+41 07 54.7	2011-08-01	Henze		flared				
0655620401	00 44 01.7	+41 04 23.8	2012-01-21	Henze	20.5 (12.5)	20.6 (12.8)	9.1 (8.7)	M	M	T1
0672130101	00 42 41.8	+40 51 54.6	2011-06-27	Wang	100.5 (85.9)	100.6 (90.8)	97.8 (53.3)	T1	T1	T1
0672130501	00 42 41.8	+40 51 54.6	2011-07-13	Wang	49.4 (27.1)	49.4 (29.6)	47.6 (12.8)	T1	T1	T1
0672130601	00 42 41.8	+40 51 54.6	2011-07-05	Wang	95.9 (74.5)	92.4 (78.9)	95.4 (58.8)	T1	T1	T1
0672130701	00 42 41.8	+40 51 54.6	2011-07-07	Wang	85.7 (78.4)	90.8 (80.1)	82.0 (62.4)	T1	T1	T1
0674210201	00 42 44.3	+41 16 09.4	2011-12-28	Pietsch	20.6 (20.6)	20.6 (20.6)	18.9 (18.5)	M	M	T1



Continuation of Table A.1

ObsID	RA	DEC	Start Date	PI	$t_{M1}^0$ (GTI)	$t_{M2}$ (GTI)	$t_{PN}$ (GTI)	filter <sub>M1</sub>	filter <sub>M2</sub>	filter <sub>PN</sub>
0674210601	00 42 44.3	+41 16 09.4	2012-01-31	Pietsch		flared				
0690600401	00 42 52.0	+41 31 07.8	2012-06-26	Barnard	114.3 (89.8)	114.4 (96.6)	103.5 (57.0)	T1	T1	T1
0700380501	00 42 43.7	+41 25 18.5	2012-07-28	Schartel	11.6 (11.6)	11.6 (11.6)	10.0 (9.9)	M	M	T1
0700380601	00 42 43.7	+41 25 18.5	2012-08-08	Schartel	20.8 (20.1)	20.2 (19.2)	19.6 (18.3)	M	M	T1
0701981201	00 44 02.0	+41 25 44.4	2013-02-08	Schartel	23.6 (19.8)	23.6 (19.8)	21.9 (17.0)	T1	T1	T1
0727960401	00 42 52.4	+41 16 31.2	2013-07-06	Schartel	10.6 (10.3)	10.6 (10.4)	9.0 (9.0)			
0744350301	00 43 26.7	+41 23 33.3	2014-08-09	Henze	23.4 (23.2)	23.4 (23.0)	21.8 (21.0)	M	M	T1
0744350901	00 43 26.7	+41 23 33.3	2015-02-01	Henze	11.3 (7.9)	11.3 (8.2)	9.9 (9.8)	M	M	T1
0761970101	00 43 37.9	+41 19 19.0	2015-06-27	Hornschemeier		flared				
0763120101	00 44 21.9	+41 31 16.6	2015-06-28	Sasaki	96.7 (95.1)	96.6 (95.2)	94.7 (85.0)	M	M	T1
0763120201	00 44 21.9	+41 31 16.6	2016-01-21	Sasaki	21.2 (8.5)	80.9 (52.5)	21.4 (10.3)	M	M	T1
0763120301	00 44 49.3	+41 49 31.1	2015-08-11	Sasaki	101.3 (100.7)	101.6 (100.9)	99.9 (96.9)	M	M	T1
0763120401	00 44 54.3	+41 49 12.7	2016-01-01	Sasaki	98.9 (69.6)	99.0 (73.2)	97.4 (50.8)	M	M	T1
0764030301	00 42 57.7	+41 08 12.3	2016-01-16	Henze		flared				
0764030401	00 42 57.7	+41 08 12.3	2016-02-09	Henze	11.1 (10.6)	11.6 (11.4)	7.0 (5.6)	T1	T1	T1
0784000101	00 45 28.8	+41 54 09.9	2016-12-26	Henze	40.5 (13.6)	40.5 (14.5)	36.1 (6.4)	T1	T1	T1
0784000201	00 45 28.8	+41 54 09.9	2016-12-28	Henze	57.5 (40.0)	58.3 (40.9)	56.0 (35.4)	T1	T1	T1
0790830101	00 43 31.9	+41 13 14.3	2017-01-21	Yukita	58.7 (39.2)	58.6 (39.5)	57.0 (36.4)	M	M	M
0800730101	00 37 02.3	+43 13 20.9	2017-06-28	Li	18.1 (15.6)	22.8 (18.5)	14.3 (6.6)	T1	T1	T1
0800730201	00 35 39.4	+42 52 34.0	2017-07-25	Li	15.6 (15.6)	15.6 (15.5)	11.7 (11.4)	T1	T1	T1
0800730301	00 34 06.2	+42 34 03.8	2017-07-14	Li	23.7 (20.4)	24.6 (23.7)	13.8 (11.5)	T1	T1	T1
0800730401	00 35 05.4	+42 11 46.9	2017-07-27	Li	15.6 (15.3)	15.6 (15.6)	11.7 (11.7)	T1	T1	T1
0800730501	00 36 27.1	+42 28 34.6	2017-07-28	Li	24.5 (17.7)	24.5 (18.6)	14.1 (11.5)	T1	T1	T1
0800730601	00 37 41.8	+42 48 47.7	2017-08-12	Li	15.6 (13.5)	15.6 (13.3)	11.1 (7.7)	T1	T1	T1
0800730701	00 38 31.0	+42 25 33.8	2017-08-12	Li	15.5 (15.4)	15.6 (15.4)	10.8 (10.8)	T1	T1	T1
0800730801	00 37 14.0	+42 09 03.0	2017-08-10	Li	15.7 (15.6)	15.7 (15.7)	11.8 (11.8)	T1	T1	T1
0800730901	00 35 55.5	+41 53 21.6	2018-01-07	Li	19.7 (19.6)	19.7 (19.6)	15.8 (14.8)	T1	T1	T1
0800731001	00 36 43.7	+41 33 24.1	2017-08-10	Li	15.6 (15.4)	15.6 (15.5)	11.7 (11.7)	T1	T1	T1
0800731101	00 39 10.6	+42 01 39.4	2018-01-07	Li	20.9 (20.7)	20.9 (20.8)	17.3 (16.5)	T1	T1	T1
0800731201	00 40 13.9	+42 22 05.6	2018-01-10	Li	17.6 (6.3)	17.6 (8.0)	4.4 (3.7)	T1	T1	T1
0800731301	00 42 27.3	+42 13 16.8	2018-01-11	Li	11.4 (10.9)	11.4 (11.1)	7.5 (6.6)	T1	T1	T1
0800731401	00 41 08.2	+41 58 34.9	2018-01-11	Li	15.2 (7.0)	15.1 (7.3)	11.7 (4.5)	T1	T1	T1
0800731501	00 38 58.6	+41 29 21.5	2017-08-12	Li	15.6 (15.5)	15.6 (15.4)	11.7 (11.4)	T1	T1	T1
0800731601	00 37 48.6	+41 12 46.3	2017-08-02	Li	21.5 (21.4)	21.5 (21.5)	17.6 (16.2)	T1	T1	T1
0800731701	00 43 24.4	+40 18 50.8	2018-01-11	Li		flared				
0800731801	00 45 00.6	+40 36 11.2	2018-01-12	Li	17.6 (3.8)	17.6 (5.4)	8.9 (0.7)	T1	T1	T1
0800731901	00 46 32.3	+40 56 27.6	2018-01-13	Li	17.6 (17.5)	17.6 (17.6)	13.7 (13.7)	T1	T1	T1
0800732001	00 47 44.2	+41 19 12.1	2018-01-13	Li	17.6 (17.6)	17.6 (17.5)	13.6 (13.5)	T1	T1	T1
0800732101	00 48 44.9	+41 00 00.0	2018-01-13	Li	19.2 (15.7)	21.1 (16.9)	16.8 (11.2)	T1	T1	T1
0800732201	00 48 06.0	+40 44 34.9	2018-01-14	Li	15.6 (10.0)	15.6 (10.2)	11.7 (5.6)	T1	T1	T1
0800732301	00 45 23.1	+40 10 48.9	2018-01-15	Li	15.6 (11.7)	15.6 (12.7)	11.7 (7.4)	T1	T1	T1
0800732401	00 47 03.6	+40 04 29.5	2018-01-15	Li	15.3 (6.0)	15.3 (6.4)	11.2 (1.8)	T1	T1	T1
0800732501	00 49 41.6	+40 42 43.4	2018-01-15	Li	16.9 (11.9)	16.9 (12.3)	12.9 (7.6)	T1	T1	T1
0800732601	00 50 32.4	+40 24 05.7	2018-01-16	Li	8.7 (6.4)	9.1 (7.9)	5.6 (3.5)	T1	T1	T1
0800732701	00 49 03.6	+40 00 34.6	2018-01-17	Li	15.6 (10.1)	15.6 (11.0)	11.6 (4.8)	T1	T1	T1
0800732801	00 48 17.8	+39 42 55.5	2018-01-17	Li	15.6 (12.3)	15.6 (12.2)	11.6 (6.7)	T1	T1	T1
0800732901	00 50 11.8	+39 49 41.7	2018-01-19	Li	15.3 (12.5)	15.3 (13.2)	11.7 (7.6)	T1	T1	T1

Continuation of Table A.1

ObsID	RA	DEC	Start Date	PI	$t_{M1}^0$ (GTI)	$t_{M2}$ (GTI)	$t_{PN}$ (GTI)	filter <sub>M1</sub>	filter <sub>M2</sub>	filter <sub>PN</sub>
0800733001	00 51 23.6	+40 05 56.9	2018-01-19	Li	11.8 (11.5)	11.8 (11.8)	11.4 (11.2)	T1	T1	T1
0800733101	00 38 31.0	+42 25 33.8	2018-01-03	Li		flared				
total					3082.9 (2491.6)	3133.9 (2602.0)	2710.2 (1927.4)			
End of Table										

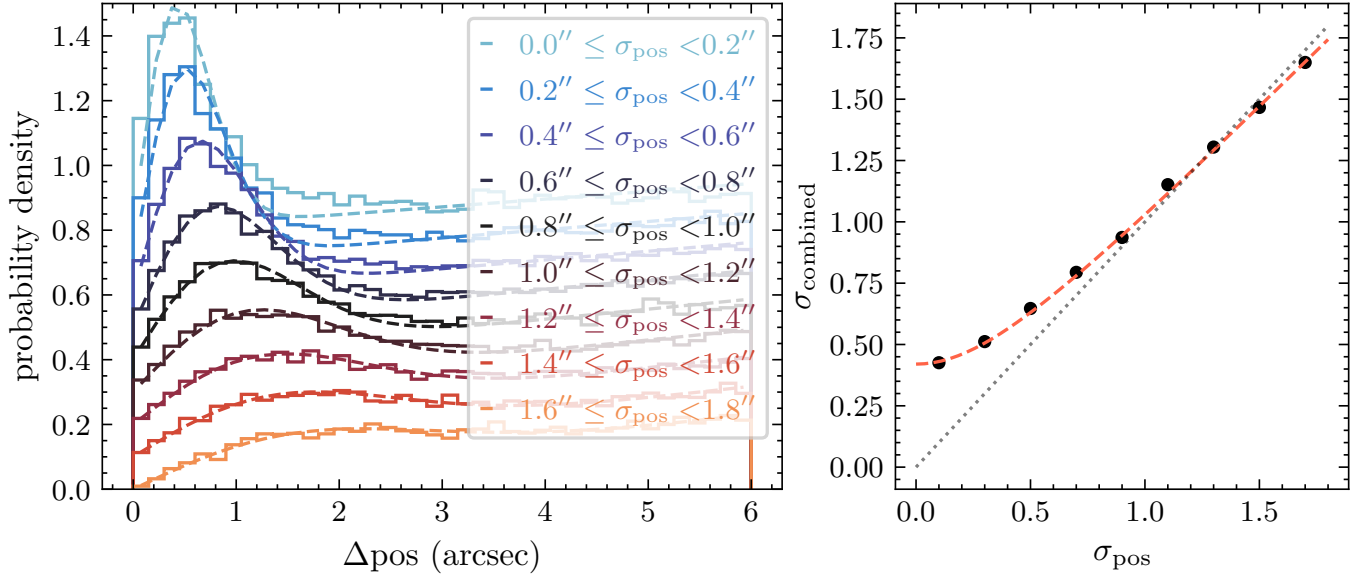


**Figure 10.** Left: The probability density function (PDF) of the offset  $\Delta\text{pos}$  between *XMM-Newton* X-ray sources and GAIA optical sources at the different ranges of the position statistical uncertainty  $\sigma_{\text{pos}}$  of the X-ray sources. The corresponding best-fit models are shown in dashed lines. The distribution have been shifted vertically for the ease of comparison. Right: Total position uncertainty  $\sigma_{\text{combined}}$  as the function of  $\sigma_{\text{pos}}$ . The  $\sigma_{\text{combined}}$  is the  $\sigma$  of Rayleigh distribution. The measured  $\sigma_{\text{combined}}$  is in black dot, while the red dashed line is the best-fit model and the black dotted line represent the uncorrected  $\sigma_{\text{pos}}$ .

## B. ASTROMETRIC ACCURACY

We initially use a  $\Delta\text{pos} < 3.44 \sigma_{\text{pos}}$  criterion to match X-ray sources, but this approach proved inadequate for exceptionally bright sources. This is due to the fact that the statistical position uncertainty,  $\sigma_{\text{pos}}$ , underestimated the actual uncertainty for these sources, resulting in failed matches. To address this issue, we match the 4XMM-DR11s serendipitous source catalogue from stacks (Traulsen et al. 2020, 2022) with GAIA DR3 catalogue (Gaia Collaboration 2022) to apply a correction to the position uncertainty. We filter the GAIA DR3 catalogue with  $G_{\text{mag}} < 18$  and  $\text{PSS} > 0.9$ , which excludes optical faint sources and limits our selection to fg stars, as some fg stars are particularly bright in X-ray observations. In Fig. 10, we clearly see the evolution of the distribution of the offset  $\Delta\text{pos}$  between the X-ray sources and GAIA sources with the position uncertainty  $\sigma_{\text{pos}}$ . The distribution can be modeled using a Rayleigh function and a proportional function. The Rayleigh function represents true counterparts, while the proportional function accounts for the false positive matches. We take the fitted  $\sigma$  of Rayleigh function as the  $\sigma_{\text{combined}}$ . The relation between the  $\sigma_{\text{combined}}$  and the statistical position uncertainty  $\sigma_{\text{pos}}$  is shown in the right panel of Fig. 10. At low  $\sigma_{\text{pos}}$ , which is often the case for bright X-ray sources, the deviation of  $\sigma_{\text{combined}}$  from  $\sigma_{\text{pos}}$  is evident. However, at the large  $\sigma_{\text{pos}}$  end,  $\sigma_{\text{combined}}$  is almost unchanged.

We fit the measured  $\sigma_{\text{combined}}$ , and get the best fit model (Equation. 1)

$$\sigma_{\text{combined}} = \sqrt{0.89 \times \sigma_{\text{pos}}^2 + 0.42^2}$$

Then we modify the matching criterion based on distance as  $\Delta\text{pos} < 3.44 \sigma_{\text{combined}}$ . Since we use the same source detection tool `edetect_stack` in this work as in 4XMM-DR11s, the empirical relation of the  $\sigma_{\text{combined}}$  can be adopted in this work.

## C. CROSS-MATCHING WITH NWAY

In our study, we utilize NWAY (Salvato et al. 2018), a Bayesian cross-matching algorithm, to match fg stars with our X-ray source list. Since it is possible for one X-ray source to match with multiple stars within the distance criterion due to the numerous stars in GAIA catalogue. NWAY takes into account positional uncertainties and assigns probabilities to potential matches based on source properties and positional agreement. The priors of these properties can be automatically assigned based on the sources of secure matches and non-matches in the field. Compared to

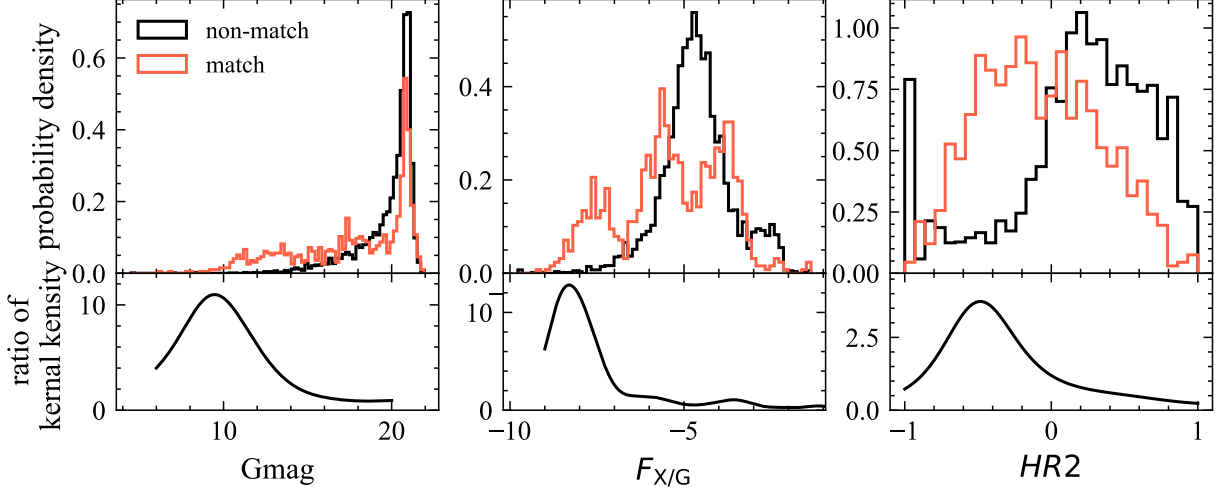


**Figure 11.** The probability density of GAIA  $Gmag$ ,  $F_{X/G}$  (flux ratio between 0.5-2.0 keV to GAIA G band), and  $HR2$  for secure matches and non-matches based on distance. Also shown are the corresponding ratio of the kernel density of these parameters.

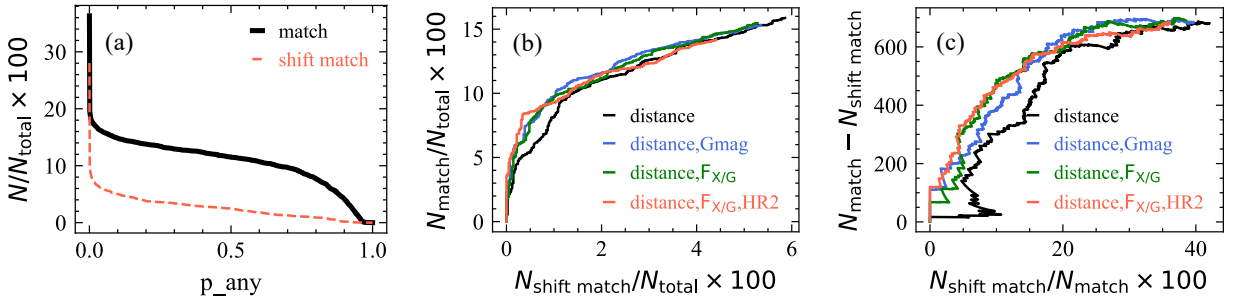


**Figure 12.** a. The fraction of matched sources and matches of shifted X-ray sources as the function of  $p\_any$  (the probability of matching defined in NWAY) based on the distance; b. The fraction of the matched sources as the function of the fraction of the matches of shifted sources; c. The estimated number of secure matches as the function of the fraction of false positive matches. In b and c, we demonstrate the comparison of matching performance between different priors: no prior (distance only),  $Gmag$ ,  $F_{X/G}$ , and  $F_{X/G}$  with  $HR2$ .

distance-based matching algorithms, NWAY can handle complex fields and provides more reliable and informative matches.

To select reference star catalogues, we filter GAIA sources with  $PSS > 0.9$ . Initially, we match GAIA sources based solely on distance and compare the GAIA parameter distributions of the matched sources with those of non-matched sources. Fig. 11 shows the parameter distributions and highlights a significant trend where counterpart stars are optically bright, have a relatively small flux ratio between 0.5-2.0 keV and GAIA G band ( $F_{X/G}$ ), and the matched X-ray source are soft.

Next, we consider  $Gmag$ ,  $F_{X/G}$ , and  $HR2$  as prior parameters and re-run the NWAY algorithm. To test the reliability of our method, we randomly shift our X-ray source list and perform matching with the same prior parameters. In Fig. 12a, we present the fraction of matched sources ( $N_{match}/N_{total}$ ) and matches to shifted X-ray sources ( $N_{shift\_match}/N_{total}$ ) as a function of  $p\_any$ .  $N_{total}$  is the total number of the X-ray sources to be matched.  $p\_any$  is the posterior probability of the X-ray source having any correct counterparts defined by NWAY. In Fig. 12b, We present the function of the fraction of matched sources as the fraction of matches to shifted sources by varying  $p\_any$ . The different priors, including no prior (distance only),  $Gmag$ ,  $F_{X/G}$ , and  $F_{X/G}$  with  $HR2$ , are compared. We estimate the true counterpart as the function of the false match fraction in Fig. 12c. Increasing the range of  $p\_any$  can include more true counterparts but comes at the cost of a higher fraction of false matches. However, there is still an upper



limit to the number of true sources. The introduction of other parameters has resulted in a noticeable improvement in matches. We can clearly observe the improvement in the matches after introducing other parameters. As  $G_{\text{mag}}$  and  $F_{X/G}$  are correlated, we ultimately choose to use  $F_{X/G}$  for its better performance. Additionally, despite HR2 not resulting in a significant improvement in the final matching performance, we still took it into consideration since it represents the X-ray color preference of stars. Ultimately, we selected  $p_{\text{any}} > 0.9$  to identify foreground stars in X-ray sources, which corresponded to only 5% of false matches.

#### D. DESCRIPTION OF THE NEW-ANGELS CATALOGUE COLUMNS

1. Column 1, SRCID: Source identifier.
2. Column 2, OBS\_ID: Identification of XMM-Newton observation.
3. Column 3, N\_OBS: Number of observations involved in the stack.
4. Column 4, N\_CONTRIB: Number of observations in which the source was fitted.
5. Column 5, N\_EXP: Number of instruments in which the source was fitted.
6. Column 6-8, RA, DEC and RADEC\_ERR: Right ascension and Declination (J2000, in degree) and square root of squared sum of their 1-sigma uncertainties (in arcsec).
7. Column 9-10, ast\_RA and ast\_DEC: Astrometry corrected Right ascension and Declination (J2000, in degree).
8. Column 11-12, RAOFFSET and DECOFFSET: RA and DEC offset of the observation preferred in 4XMM-DR12s.
9. Column 13-14, LII and BII: Galactic longitude and latitude (in degree).
10. Column 15, DIST\_NN: Distance (in arcsec) to the nearest neighbouring detected source.
11. Column 16, N\_BLEND: Number of neighbouring sources being fit simultaneously.
12. Column 17-18, 29-30, 41-42, 53-54, EP\_FLUX, PN\_FLUX, M1\_FLUX, M2\_FLUX, EP\_FLUX\_ERR, PN\_FLUX\_ERR, M1\_FLUX\_ERR and M2\_FLUX\_ERR: Total flux ( $\text{erg cm}^{-2} \text{s}^{-2}$ ) of all-EPIC, pn, MOS1, and MOS2 and their 1-sigma uncertainty in the energy range of 0.2-12.0 keV. The flux and flux uncertainty are derived from counts rates and errors according to energy conversion factors. ( $\text{ECF} = \frac{\text{count rate}}{\text{flux}}$ , in units of  $10^{11} \text{ cts cm}^{-2}/\text{erg}$ ). The factor for each detector and energy band is different depend on the detector, pattern selection and filter used during the observation. So the ECFs (fluxes and energy conversion factors) were derived with XSPEC using on-axis response matrices assuming a power law model with photon index  $\Gamma = 1.7$  and the Galactic foreground absorption of  $N_H = 7 \times 10^{20} \text{ cm}^{-2}$  (Stark et al. 1992, see also PFH2005) to be the universal source spectrum for the ECF calculation.
13. Column 19-28, 31-40, 43-52, 55-64, EP\_n\_FLUX, PN\_n\_FLUX, M1\_n\_FLUX, M2\_n\_FLUX, EP\_n\_FLUX\_ERR, PN\_n\_FLUX\_ERR, M1\_n\_FLUX\_ERR and M2\_n\_FLUX\_ERR: The flux ( $\text{erg cm}^{-2} \text{s}^{-1}$ ) of all-EPIC, pn, MOS1, and MOS2 in energy band n and their 1-sigma uncertainty. Energy band 1, 2, 3, 4, and 5 cover 0.2-0.5 keV, 0.5-1.0 keV, 1.0-2.0 keV, 2.0-4.5 keV, and 4.5-12.0 keV respectively. The flux and the flux uncertainty of all-EPIC are weighted from that of pn, MOS1, and MOS2.

$$\begin{aligned}
 \text{EP}_n\text{FLUX} = & \frac{\text{PN}_n\text{FLUX} \times (\text{PN}_n\text{FLUX\_ERR})^{-2}}{(\text{PN}_n\text{FLUX\_ERR})^{-2} + (\text{M1}_n\text{FLUX\_ERR})^{-2} + (\text{M2}_n\text{FLUX\_ERR})^{-2}} \\
 & + \frac{\text{M1}_n\text{FLUX} \times (\text{M1}_n\text{FLUX\_ERR})^{-2}}{(\text{PN}_n\text{FLUX\_ERR})^{-2} + (\text{M1}_n\text{FLUX\_ERR})^{-2} + (\text{M2}_n\text{FLUX\_ERR})^{-2}} \\
 & + \frac{\text{M2}_n\text{FLUX} \times (\text{M2}_n\text{FLUX\_ERR})^{-2}}{(\text{PN}_n\text{FLUX\_ERR})^{-2} + (\text{M1}_n\text{FLUX\_ERR})^{-2} + (\text{M2}_n\text{FLUX\_ERR})^{-2}}
 \end{aligned} \tag{D1}$$

$$\begin{aligned}
\text{EP\_n\_FLUX\_ERR} = & \left( \frac{\text{PN\_n\_FLUX\_ERR} \times (\text{PN\_n\_FLUX\_ERR})^{-2}}{(\text{PN\_n\_FLUX\_ERR})^{-2} + (\text{M1\_n\_FLUX\_ERR})^{-2} + (\text{M2\_n\_FLUX\_ERR})^{-2}} \right)^2 \\
& + \left( \frac{\text{M1\_n\_FLUX\_ERR} \times (\text{M1\_n\_FLUX\_ERR})^{-2}}{(\text{PN\_n\_FLUX\_ERR})^{-2} + (\text{M1\_n\_FLUX\_ERR})^{-2} + (\text{M2\_n\_FLUX\_ERR})^{-2}} \right)^2 \\
& + \left( \frac{\text{M2\_n\_FLUX\_ERR} \times (\text{M2\_n\_FLUX\_ERR})^{-2}}{(\text{PN\_n\_FLUX\_ERR})^{-2} + (\text{M1\_n\_FLUX\_ERR})^{-2} + (\text{M2\_n\_FLUX\_ERR})^{-2}} \right)^2
\end{aligned} \tag{D2}$$

14. Column 65-68, 79-80, 91-92, EP\_RATE, PN\_RATE, M1\_RATE, M2\_RATE, EP\_RATE\_ERR, PN\_RATE\_ERR, M1\_RATE\_ERR and M2\_RATE\_ERR: Count rate (counts s<sup>-1</sup>) of all-EPIC, pn, mos1 and mos2 detectors and their 1-sigma uncertainty.
15. Column 69-78, 81-90, 93-102 PN\_n\_RATE, M1\_n\_RATE, M2\_n\_RATE, PN\_n\_RATE\_ERR, M1\_n\_RATE\_ERR and M2\_n\_RATE\_ERR: Count rate (counts s<sup>-1</sup>) of pn, mos1 and mos2 detectors in energy band n and their 1-sigma uncertainty.
16. Column 103-110, EP\_CTS, PN\_CTS, M1\_CTS, M2\_CTS, EP\_CTS\_ERR, PN\_CTS\_ERR, M1\_CTS\_ERR and M2\_CTS\_ERR: Number of counts (counts) of all-EPIC, pn, mos1 and mos2 detectors and their 1-sigma uncertainty.
17. Column 111, 117, 123, 129 EP\_DET\_ML, PN\_DET\_ML, M1\_DET\_ML and M2\_DET\_ML: Equivalent maximum detection likelihood of all-EPIC, pn, mos1 and mos2 detectors. The likelihood is calculated as

$$\text{DET\_ML} = -\ln\left(1 - \Gamma\left(\frac{\nu}{2}, \sum_{i=1}^n \frac{\Delta C_i}{2}\right)\right) \tag{D3}$$

where  $C$  is C-statistic (Cash 1979).  $n$  is the number of images used for the detection of the same source.  $\nu$  is the degree of freedom,  $\nu = n+2$  for point source,  $\nu = n+3$  for the extend source. While combining the detection from different instrument or observations,  $\Delta C$  are summed up in equation D3. In principal, the detection likelihood also follows  $L = -\ln(p)$ , where the  $p$  is the probability of resulting in at least the observed counts by Poissonian random fluctuation. The probability  $p$  is calculated from incomplete Gamma function  $P(a, b)$ , where  $a$  is the raw source counts and  $b$  is the raw background counts in the detection cell. (For more detail of detection likelihood, see Watson et al. 2009, Traulsen et al. 2019)

18. Column 112-116, 118-122, 124-128, 130-134 EP\_n\_DET\_ML, PN\_n\_DET\_ML, M1\_n\_DET\_ML and M2\_n\_DET\_ML: Equivalent maximum detection likelihood ( $n = 1$  in equation D3) of all-EPIC, pn, MOS1 and MOS2 detectors in energy band n, n=1, 2, 3, 4 and 5.
19. Column 135-136, EXTENT and EXTENT\_ERR: Extent radius (arcsec) and its 1-sigma uncertainty. The parameters are obtained when fitting the extended source with a convolution of the instrumental PSF and an extent model ( $\beta$  model with fixed  $\beta = 2/3$ ). ( $\nu = n + 3$  in equation D3).
20. Column 137, EXTENT\_ML: Likelihood of the detection being extended when fitting with a convolution of the instrumental PSF and an extent model ( $\beta$  model with fixed  $\beta = 2/3$ ). ( $\nu = n + 3$  in equation D3).
21. Column 138-169, EP\_HRn, PN\_HRn, M1\_HRn, M2\_HRn, EP\_HRn\_ERR, PN\_HRn\_ERR, M1\_HRn\_ERR and M2\_HRn\_ERR: Hardness ratio and corresponding 1-sigma uncertainty of all-EPIC, pn, mos1, and mos2 detectors between energy band n and n+1, n=1, 2, 3 and 4. The hardness ratios are defined as:  $HR_n = \frac{B_{n+1} - B_n}{B_{n+1} + B_n}$ ,  $B_n$  is the count rate in energy band n. After computing the hardness ratios, we can plot the hardness ratio diagram to classify the spectra.
22. Column 170, 176, 182, PN\_EXP, M1\_EXP and M2\_EXP: PSF-weighted exposure time (second) of the detection in pn, mos1 and mos2.
23. Column 171-175, 177-181, 183-187, PN\_n\_EXP, M1\_n\_EXP and M2\_n\_EXP: PSF-weighted exposure (second) of the detection in energy band n of pn, mos1, and mos2.

24. Column 188, 194, 100, PN\_BG, M1\_BG and M2\_BG: Background map (counts pixel<sup>-1</sup>) at detection position on pn, mos1 and mos2.
25. Column 189-193, 195-199, 201-205, PN\_n\_BG, M1\_n\_BG and M2\_n\_BG: Background map (counts pixel<sup>-1</sup>) in energy band n of pn, mos1 and mos2 at the detection position.
26. Column 206-209, EP\_ONTIME, PN\_ONTIME, M1\_ONTIME and M2\_ONTIME: Total good exposure time (second) of all-EPIC, pn, mos1 and mos2 detectors.
27. Column 210-212, PN\_PILEUP, M1\_PILEUP and M2\_PILEUP: Estimate of the pile-up level in pn, mos1 and mos2. It is calculated in terms of source count rate and instrument readout. For point-like sources, it is defined as the source count rate times the frame time, divided by an instrument-specific pile-up threshold. For extended sources, it is derived from the source counts per instrument pixel times the frame time, divided by the number of instrument pixels covered by an image pixel and by a pile-up threshold.
28. Column 213-215, PN\_MASKFRAC, M1\_MASKFRAC and M2\_MASKFRAC: PSF-weighted detector coverage in pn, mos1 and mos2.
29. Column 216, DIST\_REF: Distance (arcmin) to the reference coordinates of the field.
30. Column 217-220, EP\_OFFAX, PN\_OFFAX, M1\_OFFAX and M2\_OFFAX: Offaxis angle (arcmin) between source position and aim point all-EPIC, pn, mos1, and mos2 detectors.
31. Column 221-235, PN\_n\_VIG, M1\_n\_VIG and M2\_n\_VIG: Vignetting factor in energy band n of pn, mos1 and mos2 detectors for the detection.
32. Column 236, STACK\_FLAG: Integer representation of the stack detection flags.
33. Column 237, OVERLAP: True, if N\_CONTRIB ≥ 2 at the source position.
34. Column 238, VAR\_CHI2: Reduced chi square of all-EPIC inter-observation variability. 
$$\text{VAR\_CHI2} = \frac{1}{n-1} \sum_{k=1}^n \left( \frac{F_k - F_{EPIC}}{\sigma_k} \right)^2$$
,  $F_k$  is EP\_FLUX for each observation,  $\sigma_k$  is EP\_FLUX\_ERR.  $F_{EPIC}$  is the mean EP\_FLUX for all detections.
35. Column 239-243, VAR\_CHI2\_n: Reduced chi square of all-EPIC band n inter-observation variability.
36. Column 244, VAR\_PROB: Probability that the all-EPIC flux variability is consistent with zero.  $\text{VAR\_PROB} = \int_{\chi^2}^{\infty} \frac{x^{\nu/2-1} e^{-x/2}}{2^{\nu/2} \Gamma(\nu/2)} dx$ ,  $\chi^2$  is VAR\_CHI2 at  $\nu = n - 1$  degrees of freedom. The high VAR\_PROB means that the flux of the source is almost constant throughout the observations.
37. Column 245-249, VAR\_PROB\_n: Probability that the all-EPIC band n flux variability is consistent with zero.
38. Column 250, FRATIO and FRATIO\_ERR: The ratio and corresponding 1-sigma uncertainty between the highest and the lowest (non-zero, non-null) mean EPIC flux.  $\text{FRATIO} = F_{\max}/F_{\min}$ ,  $F_{\max}$  and  $F_{\min}$  are the maximum and minimum of EP\_FLUX in detections.
39. Column 252-261, FRATIO\_n and FRATIO\_n\_ERR: The ratio and corresponding 1-sigma uncertainty between the highest and the lowest (non-zero, non-null) mean EPIC flux in energy band n.
40. Column 262, FLUXVAR: The Largest all-EPIC flux difference in terms of sigma. 
$$\text{FLUXVAR} = \max_{k,l \in [1,n]} \frac{|F_k - F_l|}{\sqrt{\sigma_k^2 + \sigma_l^2}}$$
,  $F_k$  is EP\_RATE,  $\sigma_k$  is EP\_RATE\_ERR.
41. Column 263-267, FLUXVAR\_n: The Largest all-EPIC band n flux difference in energy band n in terms of sigma.
42. Column 269-270, MJD\_FIRST and MJD\_LAST: Modified Julian Date JD-2400000.5 (in days) when starting and ending the observation.
43. Column 270, REVOLUT: XMM-Newton revolution number (in orbit) of the observation.

44. Column 271, `PA_PNT`: Mean position angle (degree) of the spacecraft.
45. Column 272-274, `PN_SUBMODE`, `M1_SUBMODE` and `M2_SUBMODE`: instrument submode of pn, mos1 and mos2 used for the observation.
46. Column 275-277, `PN_FILTER`, `M1_FILTER` and `M2_FILTER`: Filter used for the pn, mos1 and mos2.
47. Column 278, `type`: The identification or classification type assigned to each source. The classification types include fg star, AGN, galaxy, GIC, GCI, SNR, HMXB, LMXB, and SSS. The classification of each candidate source is enclosed within angle brackets (<>) for easy identification.
48. Column 279, `ast_type`: The same as `type`, but the source is matched with new source position (`ast_RA` and `ast_DEC`).
49. Column 280, `note`: additional comments.
50. Column 281, `XMLPt`: the source number of matched sources in [Stiele et al. \(2011\)](#).
51. Column 282, `CSC_name`: The name of the matched source in the Chandra Source Catalog Release 2.0 ([Evans & Civano 2018](#)).

#### E. AN EXAMPLE OF THE SOURCE CATALOGUE TABLE



